© 2020. Published by The Company of Biologists Ltd | Journal of Cell Science (2020) 133, jcs252064. doi:10.1242/jcs.252064

TOOLS AND RESOURCES

# An image analysis method to survey the dynamics of polar protein abundance in the regulation of tip growth

**Sarah Taheraly*,§, Dmitry Ershov‡,§, Serge Dmitrieff and Nicolas Minc¶**

## ABSTRACT

Tip growth is critical for the lifestyle of many walled cells. In yeast and fungi, this process is typically associated with the polarized deposition of conserved tip factors, including landmarks, Rho GTPases, cytoskeleton regulators, and membrane and cell wall remodelers. Because tip growth speeds may vary extensively between life cycles or species, we asked whether the local amount of specific polar elements could determine or limit tip growth speeds. Using the model fission yeast, we developed a quantitative image analysis pipeline to dynamically correlate single tip elongation speeds and polar protein abundance in large data sets. We found that polarity landmarks are typically diluted by growth. In contrast, tip growth speed is positively correlated with the local amount of factors related to actin, secretion or cell wall remodeling, but, surprisingly, exhibits long saturation plateaus above certain concentrations of those factors. Similar saturation observed for Spitzenkörper components in much faster growing fungal hyphae suggests that elements independent of canonical surface remodelers may limit single tip growth. This work provides standardized methods and resources to decipher the complex mechanisms that control cell growth.

This article has an associated First Person interview with Sarah Taheraly, joint first author of the paper.

**KEY WORDS: Cell growth, Image analysis, Polarity**

## INTRODUCTION

Cell growth is of paramount importance for cell size regulation, cytoplasmic density and tissue morphogenesis (Neurohr et al., 2019; Soifer et al., 2016; Uyttewaal et al., 2012). All living cells grow, and their growth rates may vary extensively, from slow-growing animal cells to fast-growing fungal hyphae or pollen tubes (López-Franco et al., 1994; Perez-Gonzalez et al., 2019; Qin and Yang, 2011). Although the fitness advantage of different growth properties has been discussed (Di Gregorio et al., 2016; Steinberg et al., 2017; Weiss et al., 1975), the physical and biological mechanisms titrating growth speeds remain, to date, poorly unified. This is in part because this problem has often been studied at the population level, masking individual cell behavior. These population analyses have shed important light on the essential roles of global metabolic regulation, nutrient uptake and translational control (Klumpp et al., 2013; Loewith and Hall, 2011; Yuan et al., 2013). However, the growth of individual cells ultimately involves remodeling and expansion of their surfaces, a process rather attributed to the activity of the cytoskeleton, membrane trafficking and their regulators (Horio and Oakley, 2005; Köhli et al., 2008; Martin and Arkowitz, 2014). Thus, in general, the multiple intertwined elements that can modulate cell growth have hampered our understanding of this essential process.

Growth analysis of single cells from microscopy time-lapse imaging may represent an adequate means to study this problem in quantitative terms. However, the complex 3D geometries of adherent animal cell models, featuring ruffles and curves, and their slow growth has rendered such analysis difficult, with only few recent reports directly documenting growth trajectories of individual cells *in vitro* (Cadart et al., 2018; Perez-Gonzalez et al., 2019; Son et al., 2012). Single walled cells, such as those of yeast and other fungi, are admittedly better suited given their more rapid growth, the irreversibility of their cell wall and their simpler geometries (Köhli et al., 2008; López-Franco et al., 1994; Steinberg et al., 2017). In such cells, growth most often occurs in a polarized manner at one or several localized sites, and represents the main means for those cells to reproduce, colonize or infect hosts (Riquelme et al., 2018). Tip growth may vary extensively in directionality and speeds among different species or even during the life cycles of one given species (Bonazzi et al., 2014; Kinnaer et al., 2019; López-Franco et al., 1994; Martin and Arkowitz, 2014). Which elements may set or limit tip growth speeds thus represent a fascinating problem with high relevance to the basic physiology of walled cells.

Studies in yeast and fungal hyphae have supported one dominant model in which tip growth may primarily be dictated by the cytoskeleton and secretion machineries, which promote membrane and cell wall surface expansion (Köhli et al., 2008; Martin and Arkowitz, 2014). Indeed, many early experiments have shown that complete inhibition of actin, microtubules or secretion can halt growth (Ayscough et al., 1997; Horio and Oakley, 2005). In addition, more rapid growth, for example in more mature fungal hyphae, has been associated with higher concentrations of secretory vesicles clustered in the form of a Spitzenkörper (Köhli et al., 2008). However, some rapidly growing fungal tips do not feature a Spitzenkörper, and changes in vesicle transport rates are often only weakly correlated to increase in growth speeds (Kinnaer et al., 2019). Other models have been more centered on biophysical properties of the cytoplasm and the cell wall. Walled cells feature high internal turgor pressure on the order of 0.1–1 MPa. Turgor is thought to power growth by pushing and deforming freshly synthesized cell wall, and drastic reduction of pressure can halt growth instantaneously (Bastmeyer et al., 2002; Haupt et al., 2018; Lew, 2011; Minc et al., 2009). Because turgor is isotropic, polarized remodeling of the cell wall may render it thinner and softer, thereby restricting its expansion to cell tips (Abenza et al., 2015; Davì et al., 2019, 2018). Mechanical

Université de Paris, CNRS, Institut Jacques Monod, 75013, Paris, France.
*Present address: Institut Curie, PSL Research University, INSERM U932, 75005, Paris, France. ‡Present address: Image Analysis Hub, Institut Pasteur, 75015, Paris, France.
§These authors contributed equally to this work

¶Author for correspondence (nicolas.minc@ijm.fr)

N.M., 0000-0002-5543-7950

**Handling Editor: John Heath**
**Received 22 July 2020; Accepted 14 October 2020**

Journal of Cell Science (2020) 133, jcs252064. doi:10.1242/jcs.252064

properties of the cell wall regulated by activity of synthesis and remodeling enzymes could thus contribute to set tip growth speeds. Finally, other geometrical elements, such as tip diameter, or competition between growing tips have also been correlated with growth speeds (López-Franco et al., 1994), but whether those correlations are mere consequences of a modulation of the local abundance of growth-promoting factors has remained elusive (Bonazzi et al., 2015). Thus, in general, whether faster growing tips exhibit higher amounts of cytoskeletal, membrane or cell wall regulators, or whether one or several of those elements limit growth remains unknown.

The polar growth of the fission yeast *Schizosaccharomyces pombe* has been extensively studied over past decades, providing a large set of information on the function of individual tip proteins in growth and polarity, as well as mutants with characterized defects in growth patterns (Chang and Martin, 2009; Martin and Arkowitz, 2014). *S. pombe* cells have cylindrical shapes and grow in length during the cell cycle following a reproducible pattern. Upon cytokinesis and septation, cells first grow in a monopolar manner from their old end and then switch to a bipolar growth mode after a transition termed new end take off (NETO), during which the two growing tips share the same cytoplasm content (Baumgärtner and Tolić-Nørrelykke, 2009; Horváth et al., 2013; Mitchison and Nurse, 1985). In these cells, F-actin, but not microtubules, is strictly required for growth, and mutants in actin regulators, vesicle transport, components of the exocyst or cell wall synthesis typically exhibit severe growth defects (Chang and Martin, 2009; Martin and Arkowitz, 2014). Although recent studies have pointed to plausible intricate relationships between cell size, protein synthesis and global cell elongation rates in this system (Knapp et al., 2019), to date little is understood of how individual tip growth properties may depend on the polarized recruitment of different factors that ultimately remodel the tip surface material to accommodate local expansion. In part, one difficulty has been to accurately discern individual old versus new end growth in large data sets and multiple conditions, and compute local protein abundance at each tip.

Here, we developed a semi-automated image analysis pipeline to compute and correlate the subcellular dynamics of tens of polar factors tagged with GFP at the locus and single tip growth speeds in populations of cycling fission yeast cells. Our analysis establishes the precise temporal variation in growth speeds of each tip, and suggests that co-existing tips compete for a shared pool of growth-promoting material. We identify classes of factors positively and negatively correlated with tip growth speeds, and reveal important plateau limits to tip growth that are largely independent of the amount of canonical membrane and cell wall remodeling factors. Similar findings in very rapid growing tips of *Aspergillus nidulans* suggest that such limits are likely inherent to the process of tip growth.

## RESULTS

### An image analysis platform to quantify single tip growth rates and tip protein abundance in cell populations

To study tip growth and cell polarity in fission yeast, we developed a semi-automated image analysis software to measure individual tip elongation with a temporal resolution of 5 min, and a spatial resolution of ∼50–100 nm, as well as to compute fluorescence intensity in different parts of each cell. This analysis is based on multi-stage spinning-disk confocal time-lapse microscopy, allowing the tracking of a relatively large number of cells (∼10–15) in individual experiments. The platform for image analysis is designed for simple user access and is provided as a package with examples and precise guidelines (see download link in Materials and Methods). It includes steps and dedicated interfaces for: (1) time-lapse reordering; (2) shape segmentation with multiple methods and parameters to segment cell contours based on, for example, phase contrast, DIC or fluorescence markers; (3) isolation of single cells from a pair of dividing cells; (4) extraction of geometrical features (such as length and diameter); (5) birth scar detection; and (6) definition of multiple regions of interest from which to quantify fluoresence (Fig. S1).

For analyzing single tip growth and polarity, we first optimized time-lapse imaging conditions to achieve a high level of reproducibility and minimize photodamage (Materials and Methods; Fig. 1A; Fig. S2A,B). Quantification of individual tip growth requires reliable detection of birth scars, which serve as crucial fixed fiducial marks along the cell axis. Although phase-contrast microscopy can be used to segment the whole cell contour (Bonazzi et al., 2014), we found it was insufficient to properly discern scars. We thus supplemented cells and agar pads with a low concentration of fluorescently labeled lectins that bind galactomannan and decorate the outer part of the cell wall (Davì et al., 2018; Horiseberger and Rosset, 1977). Lectin signal-based segmentation allowed us to position and track cell contours and detect birth scars through the cell cycle, and thus compute individual tip growth (Fig. 1A,B; Fig. S1E,F and Fig. S2C). Lectin addition did not affect growth and cell cycle progression (Fig. S2A,B), and also served to sharply mark the end of septation, based on the appearance of a dark band of unlabeled cell wall septum in the mid-cell region (Horiseberger and Rosset, 1977). Together, these imaging methods and analysis pipeline allowed us to film and analyze several tens of individual cell tips and to dynamically monitor their local growth and protein abundance profile with unprecedented precision and accuracy.

### Patterns of wild-type growth rates during the cell cycle

We first used this method to document and study the dynamics of individual tip growth speed changes in the wild-type (WT) cell cycle. Cells were filmed during a period of ∼5–6 h and aligned in time to synchronize the beginning and end of each cell cycle, using the sharp appearance of the dark lectin band at the end of septation (Fig. 1E; see Materials and Methods). In agreement with previous reports (Baumgärtner and Tolić-Nørrelykke, 2009; Mitchison and Nurse, 1985), we found that the old end (OE) grew immediately after septation in a near-linear manner reaching a near-constant growth speed plateau of 0.031±0.011 µm/min (mean±s.d.) after 30–50 min. The new end (NE) exhibited a different dynamic. It first displayed a short period of positive growth associated with its rapid re-inflation immediately after septation (Atilgan et al., 2015; Baumgärtner and Tolić-Nørrelykke, 2009). It then ceased growth, before taking off *de novo*, on average at ∼60 min after septation, eventually reaching a short plateau at a growth speed of 0.022±0.007 µm/min, substantially lower than that of the old end. As a result, the total cell elongation speed, computed as the sum of both individual tips, increased steadily and reached a plateau towards the end of G2/interphase. Growth phases at both ends then sharply transitioned to a simultaneous deceleration ∼120 min after septation, reaching complete growth cessation between 150 and 170 min, followed by growth resumption in the next cell cycle (Fig. 1C,D).

Patterns of individual WT tip growth were similar at 25°C and 30°C, but tips reached higher speeds at higher temperature. At 35°C, a large fraction of cells exhibited a partial monopolar phenotype with little new end growth. By comparing patterns of the laboratory WT strain with that of a prototroph strain, we found that auxotrophies did not grossly affect growth patterns and maximal

Journal of Cell Science (2020) 133, jcs252064. doi:10.1242/jcs.252064

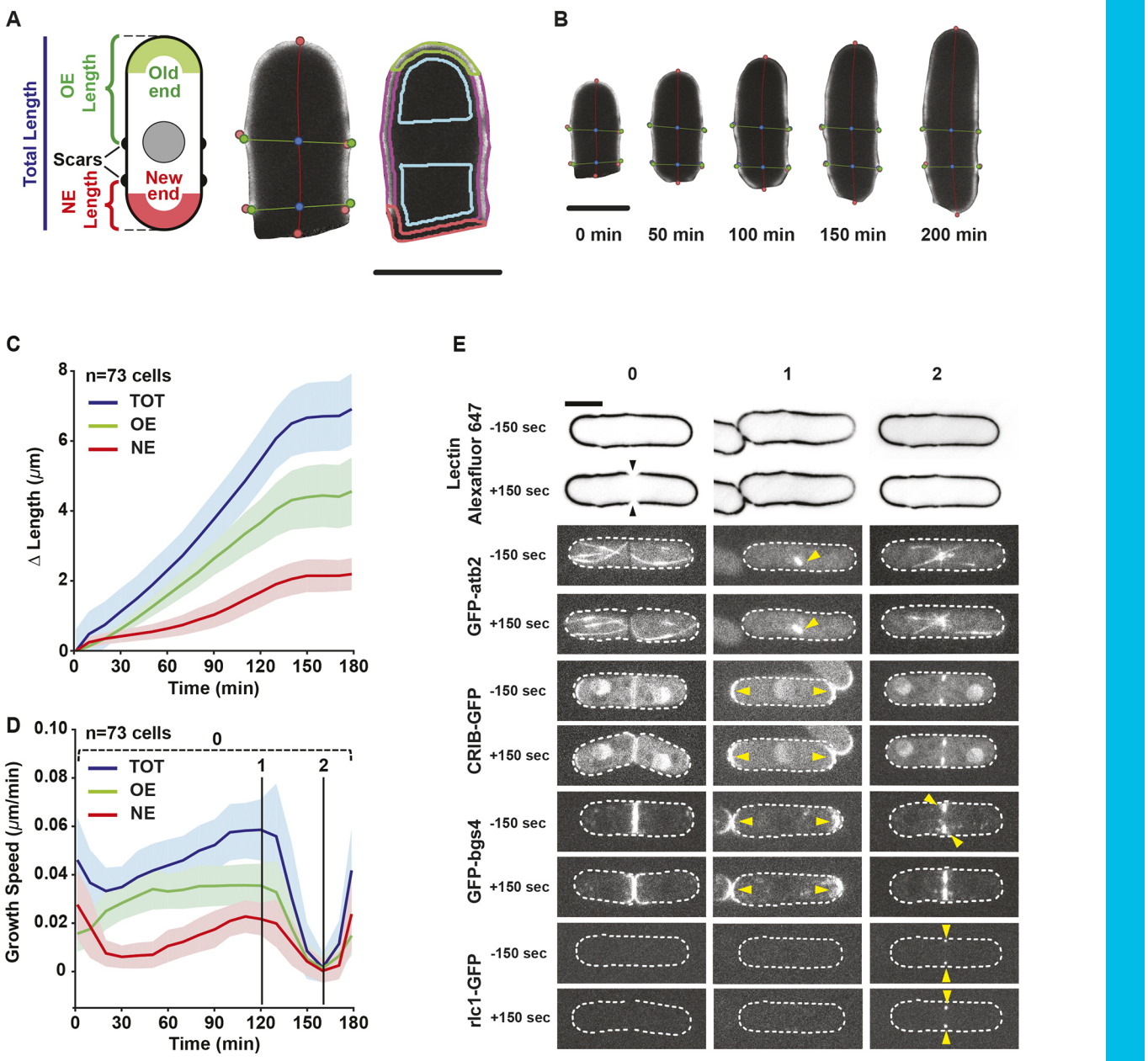


**Fig. 1. An image analysis platform to extract single tip growth trajectories in fission yeast.** (A) Left: schematic representation of a fission yeast cell with two birth scars. The green area corresponds to the old end (OE) and the red area to the new end (NE). Middle: by defining the scars from the local radius along the cell axis (colored dots at cell sides), the software extracts the evolution of each individual tip growth speed from the evolution of segments of the cell spline (red colored line along the long cell axis). Right: typical modular boxes based on the segmentation of the cell shape, which serve to compute local levels of fluorescence around the cell (green box for the old end signal, red box for the new end, purple for cell sides, and blue boxes for cytoplasm). (B) Example time-lapse images of a WT cell segmented and tracked by the software. Note how the position of the birth scars remains stable during growth over the cell cycle. (C) Length differences of growing OE, NE and total cell (TOT) for WT cells tracked every 5 min over the cell cycle. Data are represented as mean±s.d. ($n$=73 cells tracked from five independent experiments). (D) Instantaneous growth speeds, for the same set of cells as in C, computed as local derivatives of length evolution curves. The important transitions in growth speeds (0, 1 and 2) are marked in this graph and correspond to images presented in E. Stage 0 represents the end of septation, stage 1 is the maximum growth speed point, and stage 2 the lowest growth speed point. Data are represented as mean±s.d. (E) Localization of typical markers of the cell wall, mitosis, polarity, septation and cytokinesis at key transition stages in growth speeds (as indicated in D) at 150 s before and after each stage. Stage 0 marks the end of septation, as seen by the appearance of a dark band in the lectin–Alexa Fluor 647 signal (indicated by black arrowheads in the inverted images shown) and by GFP–Bgs4 decorating the full septum space. Stage 1 marks entry into mitosis, as seen in the GFP–Atb2 (microtubules) channel (arrowheads indicate an assembling mitotic spindle). Stage 2 corresponds to the initiation of cytokinesis, as seen in the CRIB–GFP, GFP–Bgs4 and Rlc1–GFP channels (arrowheads indicate the ingressing cytokinetic ring in the Rlc1–GFP channel and ingressing septum in the GFP–bgs4 channel). Dashed lines mark cell contours. Scale bars: 5 µm.

growth speeds at each tip (Fig. S2D). Also, in agreement with several reports, this analysis showed that the total growth speeds of WT cells steadily increased over the cell cycle, as cell size increased. As a consequence, the size-normalized growth rate was nearly constant during the cell cycle, in agreement with recent reports (Knapp et al., 2019). However, this rate computed for each single tip was not constant, and even decreased for the old end, suggesting that, although global cell size could participate in setting

Journal of Cell Science (2020) 133, jcs252064. doi:10.1242/jcs.252064

total cell growth speeds, individual tips may be regulated by a more local than global mechanism (Fig. S2E,F). Finally, although the mean growth speed at each tip exhibited self-similar dynamic trends in individual cells, we noted that even among cells from the same culture and filmed at the same time, there were substantial variations of up to 30–40% in individual tip growth speeds (Fig. 1D). This suggests that cell-to-cell variations in tip growth speeds, in addition to those along the cell cycle, may be exploited to understand tip growth regulation.

To identify the phases of the cell cycle associated with marked changes in tip growth speeds, we next computed growth while imaging markers of polarity (active GTP-Cdc42, using CRIB–GFP), mitosis [tubulin, using GFP–Atb2 (Tub1)], cytokinesis (myosin light chain, using Rlc1–GFP), and septation (β-glucan synthase, using GFP–Bgs4). This analysis confirmed that the time 0 of our growth curves corresponded to the end of septation, as evidenced by the GFP–Bgs4 signal that completely filled the mid-cell region (Fig. 1D,E; point 0). The onset of growth deceleration at both tips, corresponded to spindle assembly in metaphase, with the appearance of a small spindle and the absence of interphase microtubule bundles in the GFP–Atb2 signal (Fig. 1D,E; point 1). Interestingly, although growth began to decelerate at this point, we noted that both active Cdc42 and Bgs4 were still mostly present at cell tips. Finally, growth completely stalled during a short period of ∼10 min, which corresponded to the phase of ingression of the cytokinetic ring and septum (Fig. 1D,E; point 2). Accordingly, both active Cdc42 and Bgs4 became fully relocated to the mid-cell region and absent from stalled tips. Thus, entry into mitosis may trigger the progressive detachment of important polar proteins and consequent growth deceleration, with full detachment during cytokinesis and complete tip growth arrest.

### Evidence of a competition for growth potential between growing tips

One interesting feature of the WT growth pattern is that the new end never reaches the same growth speed as the old end (Fig. 1D) (Mitchison and Nurse, 1985). We envisaged three putative scenarios for this: (1) the cell cycle length may not be long enough for the new end to reach the growth speed of the old end; (2) the difference could be caused by a particular biochemistry and/or mechanics at the new end inherited from the septum (Atilgan et al., 2015; Davì et al., 2019); or (3) the two tips continuously compete for a limited pool of growth-promoting components, and the earlier take off of the old end segregates an initial pool at the expense of the new end, preventing it from reaching the same speed.

To begin testing these hypotheses, we first studied the tip growth patterns of *cdc25-22* mutant allele cells, which spend a significantly longer time in a G2 growth phase, even at a permissive temperature (25°C) (Russell and Nurse, 1986). In these cells, although the full cell cycle was much longer, NETO was delayed by a similar time as in WT cells (Fig. 2A,B). As a consequence, both tips expanded for periods twice as long as the WT expansion period, and reached growth speeds before mitosis slightly higher than those of control cells. However, despite this longer period, the new end reached a maximum growth speed plateau that was still significantly lower than that of the old end (Fig. 2C). This suggests that the duration of growth phases may not be the main factor accounting for the differential growth speeds between the old and the new end.

Next, we built on a serendipitous observation of outliers of the default growth pattern in the WT population. Because we tracked a large number of cells, we were able to find that 7% of cells exhibited a delayed bipolar pattern, in which the new end took off later than in the normal WT pattern. Remarkably, in these cells, the old end reached significantly higher growth speeds than in normal WT cells, indicating putative competitions between the two ends (Fig. 2D–F,I). Conversely, 15% of WT cells exhibited a premature bipolar pattern, in which the new end took off earlier than in the majority of WT cells. In these, the old end grew significantly slower than in the default WT pattern (Fig. 2D,G–I). Importantly, in both outlier patterns, although the distribution of growth speeds between the two ends was markedly different than in the default pattern, the growth speed of the whole cell was nearly identical (Fig. 2D–I). Thus, these observations suggest that the two ends may compete for growth potential, and that the earlier onset of *de novo* growth at the old end may provide a competitive advantage for it to reach higher speeds.

To further test this competition hypothesis, we sought to perturb the growth pattern in a more severe manner. For this, we analyzed the growth of several *tea* mutants, *tea1*Δ, *tea3*Δ and *tea4*Δ, which have penetrant monopolar phenotypes (Chang and Martin, 2009). In these cells, tip growth was monopolar and could be either restricted to the old or to the new end (Fig. 3A–F; Fig. S3A,B). In all three mutants, single growing tips, whether born from a new end or an old end, could reach maximal growth speeds that were mostly similar to each other (Fig. S3C). This observation rules out the hypothesis that inheritance of septum material at the new end could impact tip growth potential. Importantly, these individual ends grew faster than their WT counterparts. The *tea1*Δ cells provided the most striking effect, because the total cell growth speed was nearly identical to that of WT cells, so that a single old end grew ∼1.7 times faster than in WT and new ends grew up to three times faster than those in WT cells (Fig. 3F). The old and new ends of *tea3*Δ and *tea4*Δ cells also grew significantly faster than those of WT cells, but their growth speed was lower than the sum of the two ends in WT, plausibly because of secondary effects of these mutations on global processes such as metabolic activity (Fig. S3C) (Kelkar and Martin, 2015). Thus, preventing growth from one tip allows the other one to reach higher growth speeds. In conclusion, growing tips sharing the same cytoplasm may compete for a limiting pool of growth-regulating factors, and the tip that takes off earlier will maintain a growth-potential advantage over the other, even through long periods of growth.

### Dynamics of polar protein abundance and their relationship with tip growth

The above results were indicative of the existence of a putative limiting pool of one or several growth-promoting factors shared between tips. We envisaged those factors to localize at cell tips and have known contributions to polar growth. If a given factor is central to determination of tip growth speed, then one could expect that its concentration at the tip should exhibit a positive relationship with individual tip growth speeds. We thus built on our image analysis platform to extract from time-lapse movies the concentration of canonical polar proteins tagged with one or multiple GFPs at the locus. Because the global (whole-cell) concentration of many polar factors has been shown to be mostly constant over the cell cycle (Knapp et al., 2019), we focused on quantifying local polar accumulation at cell tips. The fluorescence signal at cell tips was computed as the average signal within regions of interests (boxes) of fixed sizes and normalized to that of the cytoplasm after background subtraction (Fig. S1). This normalization allowed direct subtraction of photobleaching effects from the concentration dynamics at cell tips (see Materials and Methods). In addition, cells were not necessarily filmed from the onset of septation, and were re-ordered after analysis, so that putative remaining contributions of photobleaching were likely smoothed out in our analysis. Finally, we note that this

Journal of Cell Science (2020) 133, jcs252064. doi:10.1242/jcs.252064

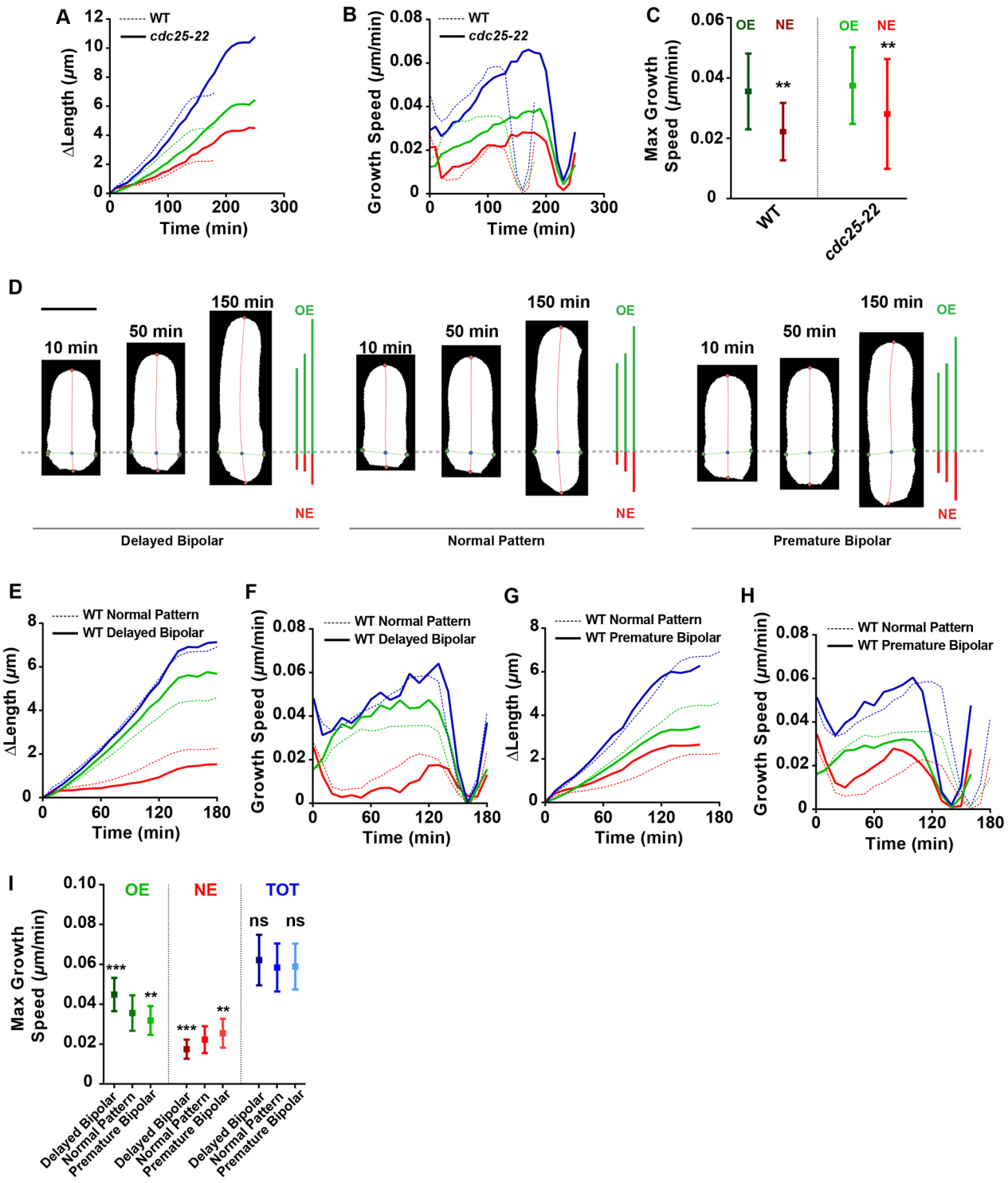


**Fig. 2. Evidence of a competition for growth potential between tips sharing the same cytoplasm.** (A,B) Comparison of total (blue), OE (green) and NE (red) length expansion (A) and growth speed (B) of WT (dotted lines, *n*=73 cells) and *cdc25-22* (full line, *n*=24 cells) cells during their respective cell cycles. (C) Mean±s.d. maximum growth speed, computed as an average over 20 min around the maximum of the speed profile, for the OE and NE of WT and *cdc25-22* cells. (D) Cell cycle time-lapse images, segmented and analyzed with our software, comparing delayed and premature bipolar patterns to canonical WT growing cells (normal pattern). The green and red lines compare growth at the OE and the NE, respectively, and black dotted lines mark the position of the birth scars. (E–H) Total (blue), OE (green) and NE (red) length expansions (E,G) and growth speeds (F,H) over the cell cycle of WT cells undergoing delayed (E,F, *n*=5 cells) and premature bipolar (G,H, *n*=11 cells) growth pattern compared to the WT normal pattern (*n*=73 cells). (I) Mean±s.d. maximum growth speed, for delayed bipolar, normal and premature bipolar cells, for the OE, NE and total (TOT). ***P*<0.01; ****P*<0.001; ns, not significant (two-tailed Mann–Whitney test). Scale bar: 5 µm.

measured concentration only represents a relative value, because some less abundant factors were tagged with multiple copies of GFP (see Materials and Methods).

We first investigated the dynamics of the most upstream landmark proteins, Tea1, Tea4 and Pom1, which are required for NETO (Fig. 4A,B) (Chang and Martin, 2009). In agreement with

Journal of Cell Science (2020) 133, jcs252064. doi:10.1242/jcs.252064

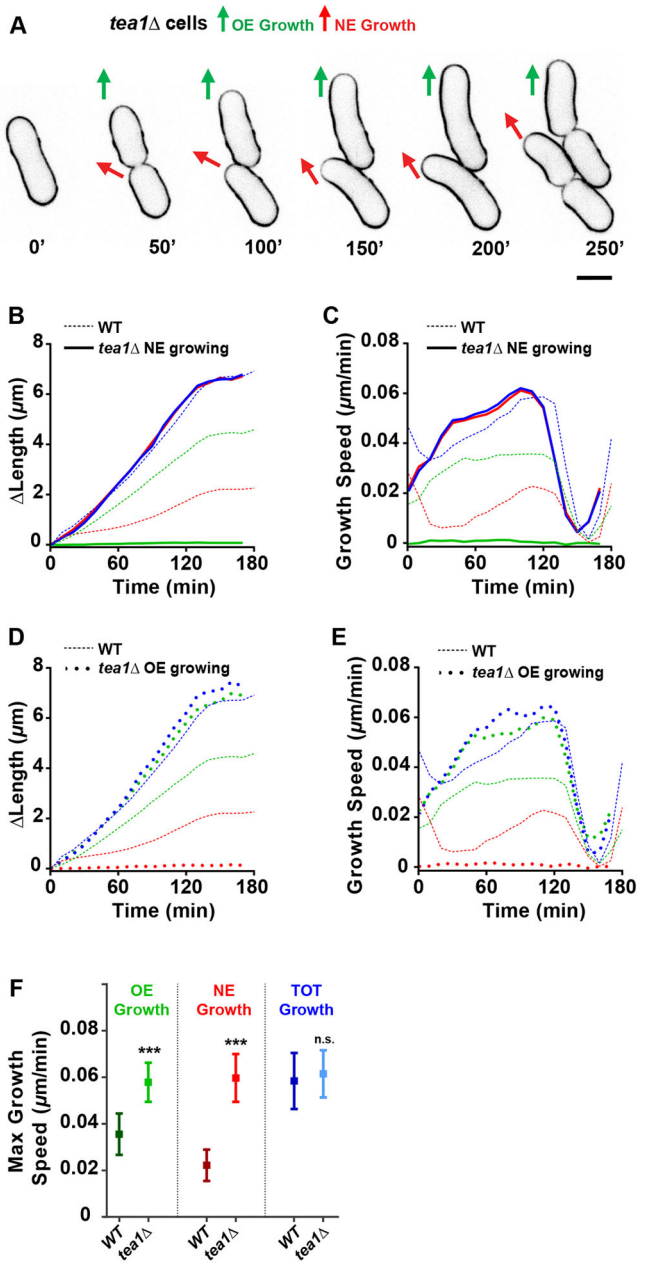


**Fig. 3. Evidence of competition for growth potential between tips in monopolar mutants.** (A) Time-lapse images of *tea1*Δ cells labeled with lectin–A647, with one daughter growing exclusively from the OE, and one from the NE. Arrows indicate direction of growth. (B–E) Length expansion and related growth speeds of *tea1*Δ cells growing from the NE only ($n$=35 cells; B,C) or the OE only ($n$=16 cells; D,E), compared with those of WT cells ($n$=73 cells). Green, OE; red, NE; blue, total. (F) Mean±s.d. maximum growth speed for OE, NE and total (TOT) length of *tea1*Δ and WT cells. ***$P$<0.001; ns, not significant (two-tailed Mann–Whitney test). Scale bar: 5 µm.

their function as landmarks promoting NETO, we found that the concentration of these factors at the new end increased over the cell cycle. For instance, Tea1–3GFP was progressively recruited to the new end after septation, and reached a saturating level typically after NETO. In sharp contrast, its concentration at the old end decreased over the cell cycle. Tea4–GFP levels were steadier at both ends, with a notable progressive recruitment at the new end. Pom1–GFP concentration also decreased steadily at the old end, and exhibited a bell-shaped curve – first increasing and then decreasing at the new end (Fig. 4C–E). To understand whether these factors could contribute to setting or limiting individual tip growth speeds, we extracted instantaneous tip factor concentration and growth speed from both tips of each cell, and binned them to plot the growth speed of a single tip (OE or NE) with respect to tip factor concentration. Importantly, the range of tip speeds and protein concentrations in these plots reflects cell-to-cell variation as well as variation along the cell cycle. Interestingly, this analysis indicated that tip speed was mostly independent of polarity landmarks, or that these were even less concentrated in tips that grew faster (Fig. 3C–E). Thus, this suggests that polar landmarks are diluted by growth, rather than contributing to growth speed per se.

Because F-actin is known to be essential for cell growth in *S. pombe*, we next looked at actin-regulating factors (Fig. 5A). One prime upstream regulator of actin assembly is the conserved Rho-GTPase Cdc42. We imaged the probe CRIB–GFP, which labels active GTP-Cdc42 (Tatebe et al., 2008). The mean dynamic of CRIB–GFP at each end over the cell cycle resembled that of the mean growth patterns, with a rising phase at the old end followed by a plateau and a sharp decay at mitosis. At the new end, CRIB–GFP concentration slowly raised from the onset of NETO and reached a plateau of concentration at a value similar to that of the old end (Fig. 5B). Accordingly, the growth speed versus concentration plot exhibited a general positive correlation, with faster growing tips associated with more CRIB–GFP signal, in agreement with the well-established role of active Cdc42 in polar growth (Martin and Arkowitz, 2014). However, we noted two unexpected features. First, the concentration of active Cdc42 at new ends covered a similar range as that at old ends, but with markedly slower growth speeds. Second, for each tip, the growth speed exhibited a long plateau over a two- to three-fold range of CRIB–GFP levels (Fig. 5B). Thus, instantaneous tip concentration of active Cdc42 cannot predict tip growth speeds, with different speeds obtained from one given tip concentration, and a single maximum growth speed across a large range of concentration values.

In agreement with the results obtained for active Cdc42, we found similar trends and dosage dependence for the formin For3 (imaged using For3–3GFP), which nucleates actin cables, and Bud6 (also known as Fat1; imaged using Bud6–3GFP), an actin nucleation-promoting factor (Chang and Martin, 2009). Both exhibited a dynamic loading at individual tips that resembled that of individual tip growth, and a long plateau in the growth speed versus concentration plot, suggesting that higher recruitment of these factors cannot improve tip growth further (Fig. 5C,D). We also investigated the dynamics of F-actin using the probe LifeAct–GFP. Importantly, the signal we analyzed mostly corresponded to bright and intense actin patches labeling endocytic vesicles, with only negligible contributions from actin cables. The dynamics of F-actin also resembled that of tip growth, and a clear saturation in growth speeds at both ends was evident for the largest range of F-actin tip concentration (Fig. 5E). Thus, although F-actin is required for growth in those cells, its local tip concentration may not limit tip growth.

We then looked at upstream factors involved in surface remodeling, covering processes including secretory vesicle delivery and fusion with the membrane, cell wall synthesis and cell wall integrity (Fig. 6A). The type V myosin Myo52 (imaged using Myo52–3GFP), which drives secretory vesicles to the cell tips, as well as Sec8 (Sec8–GFP), a subunit of the exocyst complex that promotes vesicle fusion, had signatures similar to those of the actin-related factors discussed above (Fig. 6B,C). Factors related to cell wall synthesis, including the Rho-GTPase Rho1 (visualized with the active probe act-Rho1–Citrine) and the β-glucan synthase catalytic subunits Bgs1 and Bgs4

Journal of Cell Science (2020) 133, jcs252064. doi:10.1242/jcs.252064

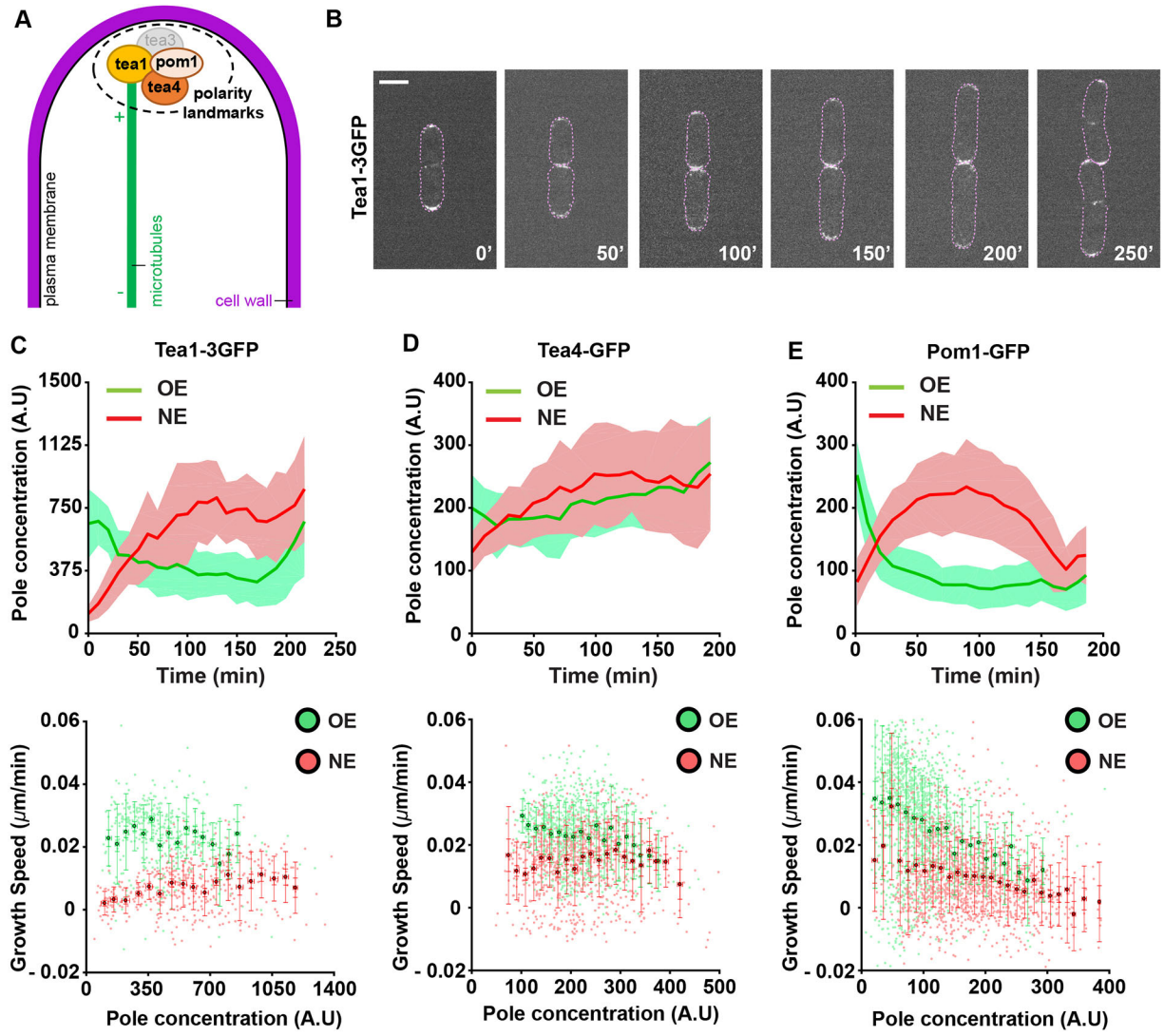


**Fig. 4. Dynamics of polar landmarks and their relation to tip growth.** (A) Schematic representation of microtubule-dependent polarization. Tea1 is deposited at the cell surface by microtubule plus ends and recruits Tea4, which recruits the DYRK-family kinase Pom1. These landmarks act as key regulators of polarity, in part by recruiting and activating downstream elements of actin-based polarity and trafficking. (B) Time-lapse images of a WT cell expressing Tea1–3GFP and stained with fluorescent lectins growing over the cell cycle. The lectin signal is represented by dotted lines to facilitate the visualization of Tea1–3GFP. (C–E) Top: evolution of the concentration of (C) Tea1–3GFP ($n$=28 cells), (D) Tea4–GFP ($n$=42 cells) and (E) Pom1–GFP ($n$=38 cells) at the OE and the NE over the cell cycle. Data are presented as mean±s.d. from at least two independent experiments. Bottom: tip growth speeds as a function of concentrations at cell poles for Tea1–3GFP, Tea4–GFP and Pom1–GFP for the OE and NE. Small dots are single time points from individual time-lapse images, large dots are binned averages and error bars represent the s.d. (see Materials and Methods for details on binning). A.U, arbitrary units. Scale bar: 5 µm.

(visualized using GFP–Bgs1 and GFP–Bgs4, respectively), also exhibited similar dynamics resembling that of tip growth, with a positive correlation with tip growth and a saturation plateau. However, we noted that GFP–Bgs1 had a more linear dose-dependent relationship with new end growth speeds, but still exhibited a plateau in growth speed at the old end (Fig. 6D–F). Finally, we also imaged the dynamics of Rgf1 (using Rgf1–GFP), an important component of the cell wall integrity pathway – a sensing cascade that controls cell wall synthesis in response to damage (Perez and Cansado, 2010). The growth speed versus concentration plot for Rgf1 was slightly different to those of all other upstream cues, and appeared to exhibit the most linear trend for both old and new ends. However, the same concentration of Rgf1–GFP did not correspond to the same tip growth speed at the new versus old end, suggesting that Rgf1 may not directly dictate growth speeds (Fig. 6G). Rather, one plausible interpretation of this curve, in line with the wall sensory function of Rgf1, is that it reflects the role of Rgf1 as a sensor of growth speed changes that accumulates at or detaches from the cell wall in response to intrinsic changes in wall strain rates (Davì et al., 2018). In conclusion, these data strongly support that canonical cell surface remodelers are positively coupled to tip growth speed, but do not directly limit it.

### Dynamics of upstream polar components in faster growing tips

To further test inherent limits to tip growth independent of canonical surface remodeling factors, we explored the dynamics of CRIB–GFP, LifeAct–GFP, Myo52–3GFP, GFP–Bgs4 and Rgf1–GFP in *tea1*Δ cells, in which individual tips can grow significantly faster than in WT (Fig. 3B–F). In these monopolar cells, all the above factors were solely located to the growing end (Fig. 7A). However, and in agreement with results in WT, the growth speed versus concentration curves of

Journal of Cell Science (2020) 133, jcs252064. doi:10.1242/jcs.252064

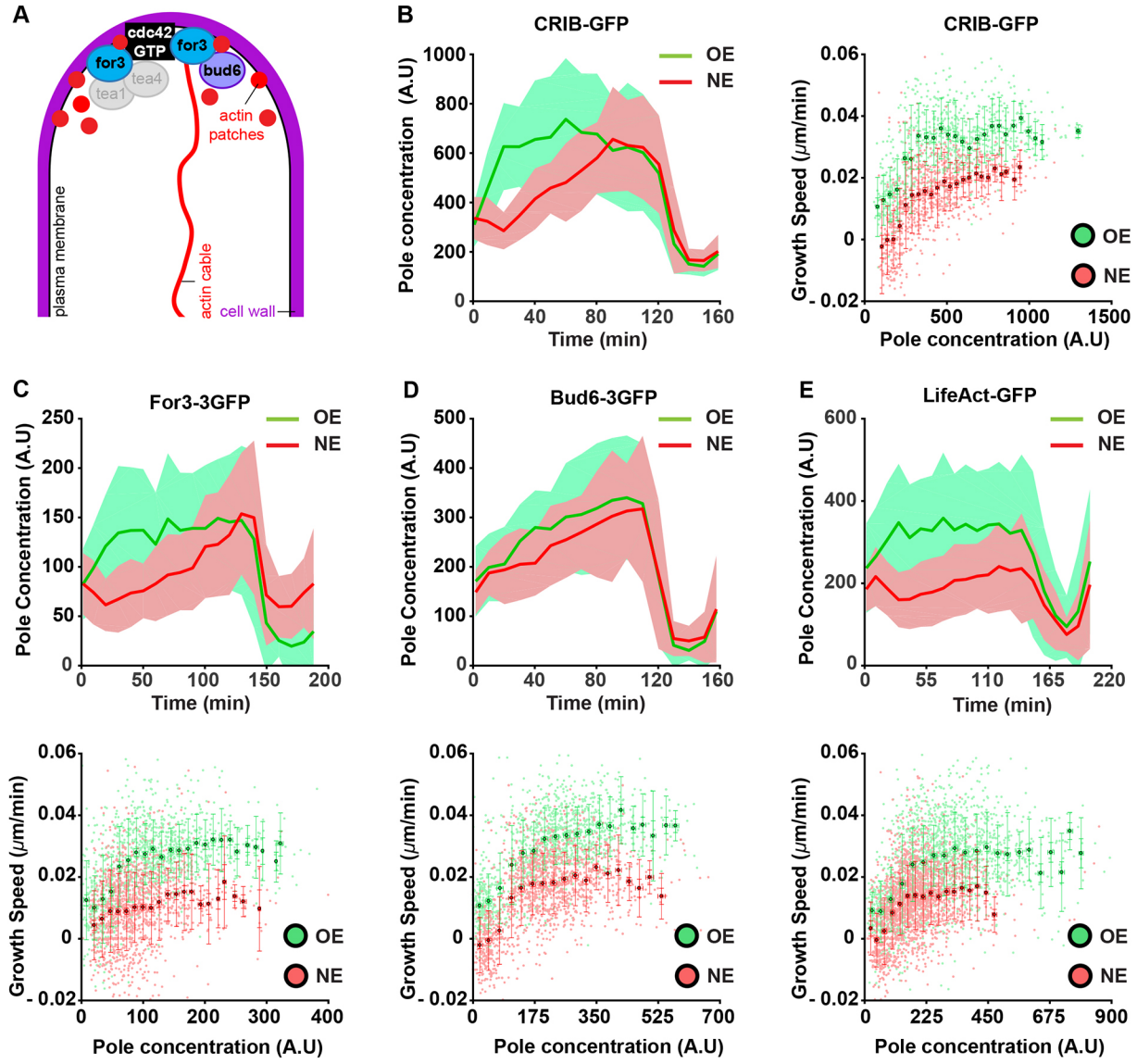


**Fig. 5. Dynamics of polar F-actin and F-actin regulators, and their relation to tip growth.** (A) Schematic representation of polar actin assembly. F-actin is present in both endocytic actin patches and cables. For actin assembly, active GTP-Cdc42 may recruit and activate multiple F-actin effectors, including the formin For3, which binds the actin-binding protein Bud6, and nucleates actin cables. (B–E) Evolution of the concentration of active Cdc42 visualized using (B) CRIB–GFP ($n$=26 cells), (C) For3–3GFP ($n$=32), (D) Bud6–3GFP ($n$=44) and (E) F-actin visualized using LifeAct–GFP ($n$=44) at the OE and the NE over the cell cycle, and tip growth speeds plotted as a function of concentrations at cell poles for the same markers. Data in concentration versus time plots are represented as mean±s.d. In speed versus concentration plots, small dots in the background are single time points from individual time-lapse images, large dots are binned averages and error bars represent the s.d. (see Materials and Methods for details on binning). A.U, arbitrary units.

CRIB–GFP, LifeAct–GFP, Myo52–3GFP and GFP–Bgs4 were shifted upward with respect to WT but still saturated across a long plateau of concentration values. Thus, for a given tip concentration of F-actin or Bgs4, for instance, a single tip can typically grow two to three times faster (Fig. 7B–E). Rgf1–GFP dynamics further supported its putative sensing phenotype, having a near-linear positive relationship with the higher tip growth speeds in *tea1*Δ cells (Fig. 7F).

Finally, we sought to further expand the range of our observations, by testing correlations between tip concentration of surface remodelers and growth speeds in much faster growing cells. For this, we adapted our image analysis platform to hyphal cells of the model filamentous fungus *A. nidulans*. Because these single tips grow rapidly and in a monopolar manner, contour detection based on phase-contrast images was sufficient to compute instantaneous growth speeds (Fig. 8A,B). In these hyphal cells, the Spintzenkörper is an established source of local secretory vesicles needed for surface remodeling, therefore we tracked GFP–RabE$^{Rab11}$, which labels exocytic post-golgi vesicles and thus represents a faithful marker of Spintzenkörper dynamics and surface remodeling (Pantazopoulou et al., 2014; Peñalva et al., 2017). In *A. nidulans*, as in many fungi, tip growth typically increases with the age of the colony and/or the length of the hyphal compartment (Horio and Oakley, 2005; López-Franco et al., 1994). We thus filmed and computed hyphal tip growth in early germling tubes that emerge from germinating spores and precede the first septation, as well as more mature hyphae (Fig. 8A,C). This allowed our observations to span a range of ∼5–10-fold in individual tip growth speeds and almost 20–30-fold in local GFP–RabE$^{Rab11}$ concentration. Remarkably, the growth versus concentration curve for germlings resembled that of *S. pombe* individual cell tips, with a dose-dependent increase of tip growth with increasing GFP–RabE$^{Rab11}$ concentration at low

Journal of Cell Science (2020) 133, jcs252064. doi:10.1242/jcs.252064

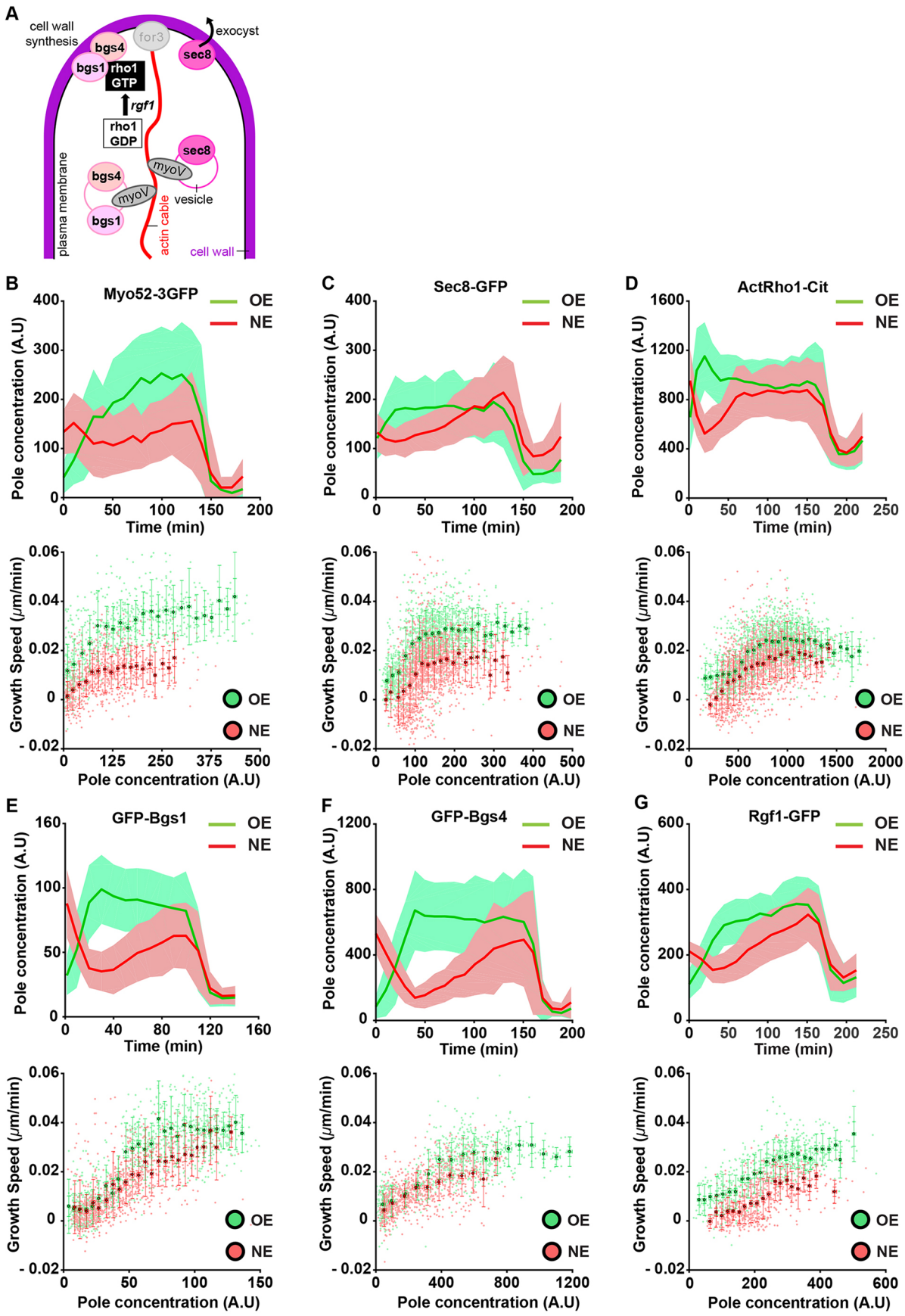


**Fig. 6.** See next page for legend.

Journal of Cell Science (2020) 133, jcs252064. doi:10.1242/jcs.252064

**Fig. 6. Dynamics of upstream polar membrane and cell wall remodelers and their relation to tip growth.** (A) Schematic representation of secretory vesicle trafficking driven by myosin type V (myoV) to the cell tips along actin cables. Vesicle fusion with the membrane is catalyzed by components of the exocyst, such as Sec8. Secretory vesicles carry enzymes for cell wall assembly, such as the β-glucan synthases Bgs1 and Bgs4, which are regulated by the small GTPase Rho1, activated by the guanine-nucleotide-exchange factor Rgf1. (B–G) Evolution of the concentration of (B) Myo52–3GFP ($n$=38 cells), (C) Sec8–GFP ($n$=40), (D) active Rho1 marked with act-Rho1–Citrine ($n$=34), (E) GFP–Bgs1 ($n$=31), (F) GFP–Bgs4 ($n$=36) and (G) Rgf1–GFP ($n$=40) at the OE and the NE over the cell cycle, and tip growth speeds plotted as a function of concentration at cell poles for the same markers. Data in concentration versus time plots are represented as mean±s.d. In speed versus concentration plots, small dots in the background are single time points from individual time-lapse images, large dots are binned averages and error bars represent the s.d. (see Materials and Methods for details on binning). A.U, arbitrary units.

and intermediate concentrations, followed by a plateau at higher concentrations (Fig. 8D). In mature hyphae, growth speed was constant over a plateau covering the full range of GFP–RabE$^{Rab11}$ concentrations. Thus, this result indicates that tip growth speeds in rapid hyphal cells, as in slower yeast cells, may also be positively correlated with, yet not limited by, the local concentration of secretory vesicles.

## DISCUSSION

### A new method to study tip growth

We here developed and validated a standardized methodology to track individual trajectories of single tips while computing the abundance of fluorescently tagged proteins. This method is based on simple confocal time-lapse imaging, and allows computation of single tip growth properties in polar-growing cells, including yeast and filamentous fungi, with medium throughput. A first particular feature that demarks our method from previously reported tracking tools for fission yeast growth (Baumgärtner and Tolić-Nørrelykke, 2009; Knapp et al., 2019; Nobs and Maerkl, 2014) is that it allows the faithful detection of birth scars, thus allowing for the study of individual tip growth in the same cell. In addition, the use of multiple detection boxes allows the computation of protein abundance at cell tips, or at any location around the cell (cytoplasm, nucleus or membrane). As exemplified in this work, this approach provides unprecedented details of polar protein dynamics and single tip growth rates, and their evolution over the cell cycle, in multiple conditions and in relatively large cell populations. Importantly, the image analysis platform has been optimized to ensure ease of user adaptation, and is readily available for the community (see download link in Materials and Methods). Thus, we anticipate that this tool will help screening of growth and polarity defects in large sets of mutants or fungal species, as well allowing better documentation of links between local or global protein abundance and morphogenetic phenotypes.

### Competition for growth potential between multiple sites

Cdc42-based polarity machineries allow cells to grow from one or multiple sites sharing the same cytoplasm (Das et al., 2012; Martin, 2015; Wu and Lew, 2013). This is typical in fission yeast during NETO, as well as in most filamentous fungi that undergo apical or lateral branching (Chang and Martin, 2009; Riquelme et al., 2018). Although mechanisms that allow for the co-existence of competing polarity domains are beginning to be understood (Bendezú et al., 2015; Howell et al., 2009), a largely unexplored question is whether multiple sites may also compete for growth potential. By tracking dynamics of single tips in outliers of the canonical fission yeast growth pattern, as well as in monopolar mutants, we reveal that growth sites sharing the same cytoplasm compete for growth potential. As a consequence, a single tip will typically grow nearly as fast as the sum of two co-growing tips in the same background. Interestingly, this competition appears to be set by the history of growth sites, rather than by an instantaneous redistribution of growth potential. Accordingly, tips that initiate growth earlier maintain an advantage for several hours and systematically reach higher speeds (Figs 2, 3). In filamentous fungi, the mother filament also grows much faster than emerging lateral branches, suggesting that this effect could represent a general feature of competing growth sites (Riquelme and Bartnicki-Garcia, 2004). One plausible interpretation is that growth initiation implicates the modification of a pre-existing non-growing membrane and cell wall, and thus consumes growth-promoting factors, thereby reducing the subsequent growth potential of the tip. We do not favor this hypothesis, because monopolar mutants like *tea1*Δ can reach similar growth speeds when growing from the former septation site (new end) or the former old end. An alternative plausible scenario is that each tip can increase their growth with a similar acceleration potential, and reach a plateau in growth speeds when a putative pool of factors promoting acceleration becomes depleted. Growth acceleration could, for instance, be associated with positive feedback between growth and polarity, which has been evidenced in fission yeast (Bonazzi et al., 2014; Haupt et al., 2018). Although computing acceleration with high accuracy, as the second derivative of length evolution, is challenging in slow-growing yeasts, we expect that such hypothesis could be easier to test in faster growing model fungi.

### Tip growth speed determination and local abundance of polar factors

The process of tip growth is intrinsically linked with the deposition of tens of different conserved factors at cell tips. The hierarchical role of each type of protein has been well established by genetic studies in model yeasts and fungi (Martin and Arkowitz, 2014; Riquelme et al., 2018). First, spatial landmarks position the incipient growth site and recruit downstream polarity components organized around the active form of Rho GTPases, such as Cdc42. Polarity platforms then localize sites of F-actin assembly, endocytosis and secretory vesicle delivery, which ultimately deliver membrane and wall remodeling factors that accommodate surface expansion. Here, by systematically documenting the dynamic loading of canonical markers of the abovementioned processes, we assessed how their polar concentration may contribute to and/or limit tip growth speed.

One general finding is that polarity landmarks appear to be rather diluted by growth, whereas other upstream elements are mostly positively correlated with growth speeds. It is possible that these differences reflect the cytoskeletal elements that drive their polar recruitment: microtubules for polar landmarks and F-actin for upstream factors. The positive relationship between upstream elements, such as F-actin, exocyst components or cell wall synthases, and single tip growth is consistent with recent reports demonstrating that an increase in proteome concentration may drive faster global cell growth (Knapp et al., 2019). However, one unexpected result is that these upstream elements do not appear strictly limiting for the determination of single tip growth speed. This result is supported by the relatively long plateaus in the growth versus concentration plots for these factors (Figs 4, 5) and by the marked difference in tip growth speed that can be achieved with a similar range of factor concentration in WT cells versus monopolar *tea1*Δ cells. We note, however, that a major limitation inherent to our approach is that we solely imaged relatively abundant and

Journal of Cell Science (2020) 133, jcs252064. doi:10.1242/jcs.252064

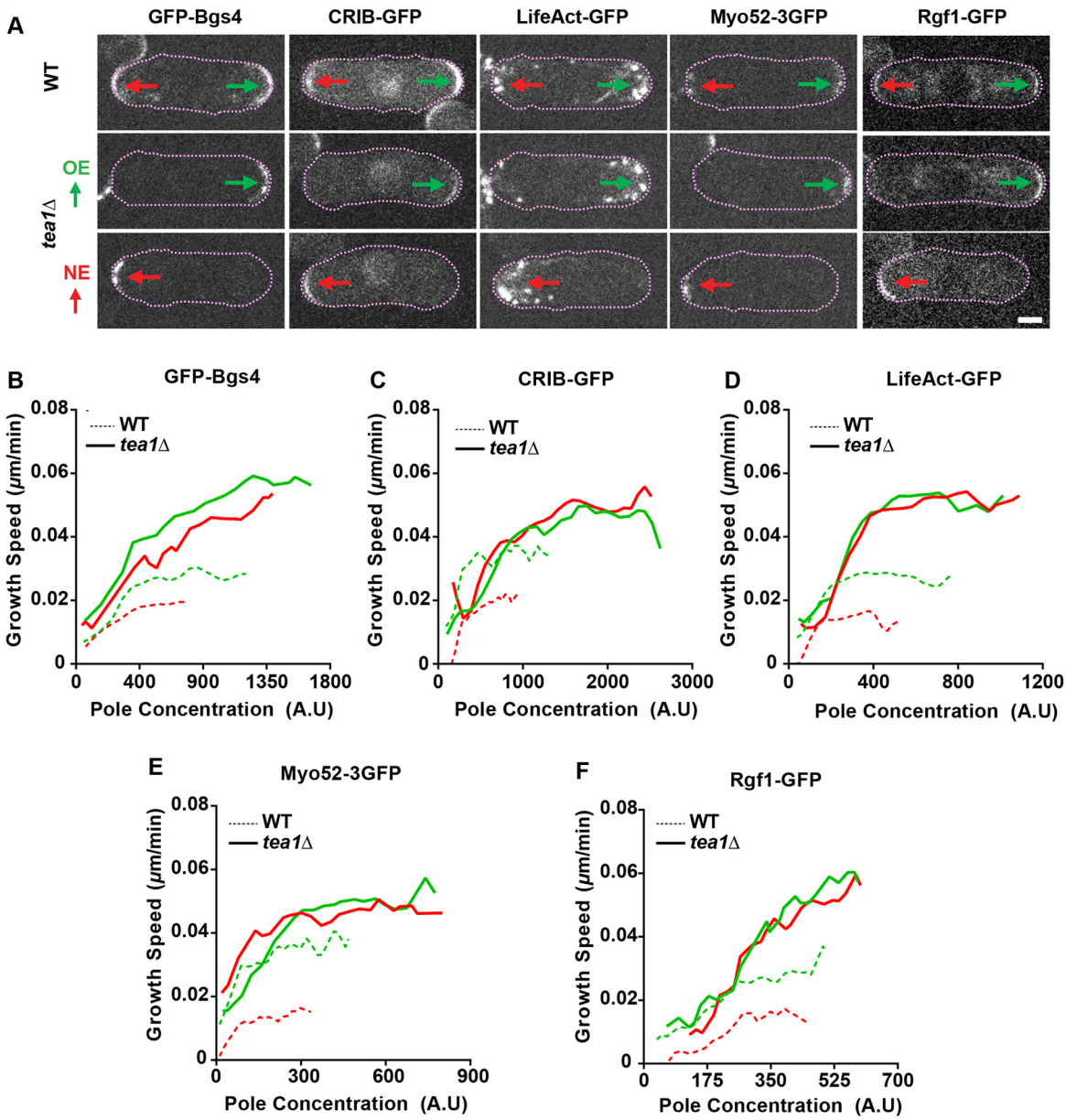


**Fig. 7. Dependence of single tip growth speed on canonical surface remodelers in bipolar and monopolar cells.** (A) Localization of the indicated polar factors in WT cells and *tea1*Δ monopolar cells growing from the OE or the NE (arrows). These cells were labeled with a fluorescent lectin, which is traced with dotted lines to facilitate the visualization of polar factors at cell tips. The fluorescence signal was contrasted, and a noise filter was applied to all these images in the same manner, for better visualization. (B–F) Single tip growth speeds plotted as a function of concentration at cell poles in WT cells and *tea1*Δ monopolar cells at the OE (green) and the NE (red), for GFP–Bgs4 (WT, *n*=36 cells; *tea1*Δ OE, *n*=24; *tea1*Δ NE, *n*=12), active GTP-Cdc42 marked with CRIB–GFP (WT, *n*=26; *tea1*Δ OE, *n*=25; *tea1*Δ NE, *n*=21), F-actin marked with LifeAct–GFP (WT, *n*=44; *tea1*Δ OE, *n*=30; *tea1*Δ NE, *n*=25), Myo52–3GFP (WT, *n*=38; *tea1*Δ OE, *n*=14; *tea1*Δ NE, *n*=16). The full and dotted lines represent the mean of binned data. A.U, arbitrary units. Scale bar: 5 µm.

previously characterized factors, thereby potentially omitting less expressed or as-yet-unidentified elements that could act as crucial limiting regulators of tip growth. For instance, our trials to properly compute the dynamics of important cell wall regulators, such as glucanases or glycosyltransferases (Davì and Minc, 2015; Perez and Ribas, 2004), failed given their low fluorescence signals. Further optimization of fluorescence tagging, or use of more advanced fluorophores, could potentially allow analysis of the contribution of these factors. In addition, growth limitation may also implicate posttranslational modifications such as phosphorylation, which we have not investigated here.

Overall, our findings suggest that the competition for growth potential between tips, or more generally the speed determination of a single growing tip, may not solely result from a simple linear competition or loading of a given pool of polar factors. Rather, these processes may implicate more complex dynamic feedbacks inherent to the polarity circuit, such as oscillations between tips (Das et al., 2012), or to cell wall rheology and assembly, which ensure surface integrity while promoting its expansion (Davì et al., 2018). Further quantitative studies of the process of cell growth will be required to decipher these complex interplays.

Journal of Cell Science (2020) 133, jcs252064. doi:10.1242/jcs.252064

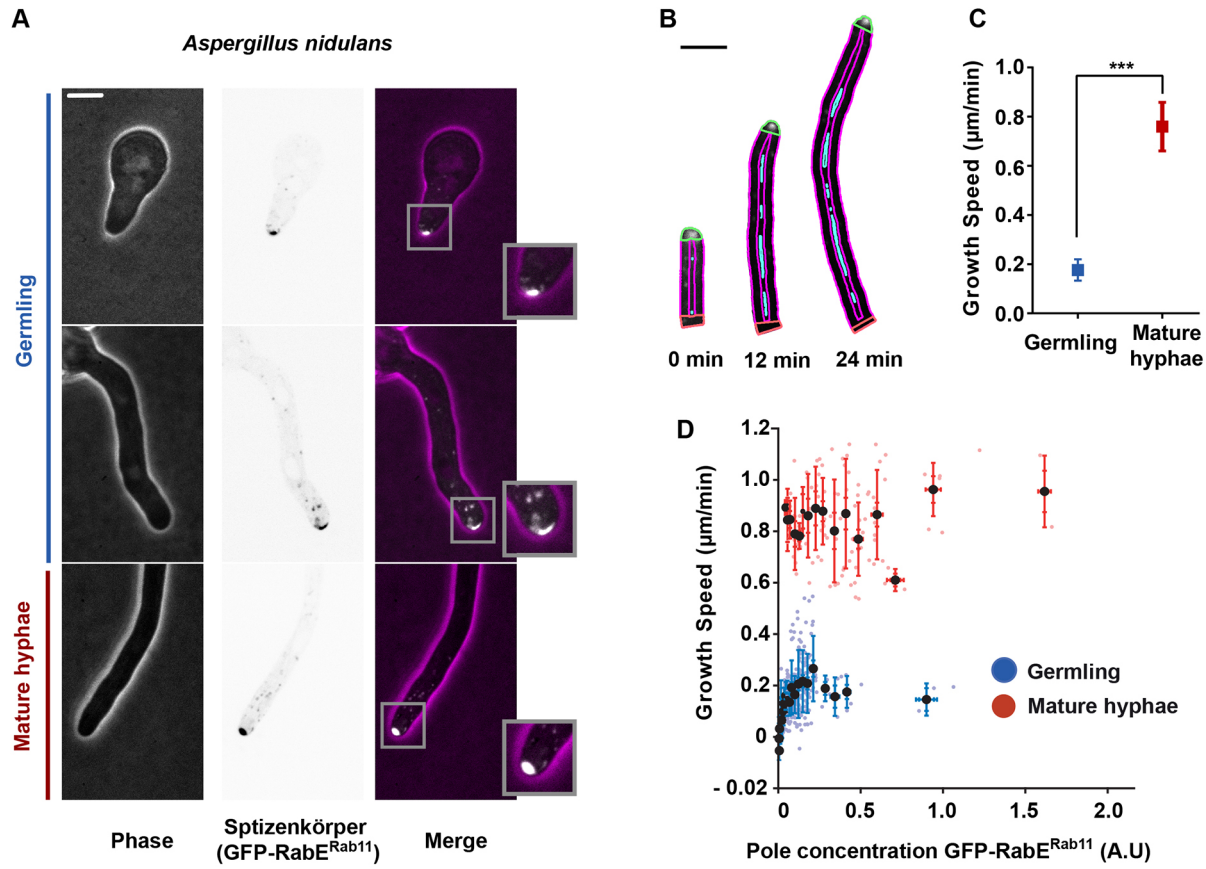


**Fig. 8. Dependence of single tip growth speed on Spitzenkörper concentration in fast growing *A. nidulans* hyphae.** (A) Images of germlings and mature hyphae, and the Spitzenkörper visualized with the post-golgi marker GFP–RabE$^{Rab11}$. Boxes indicate regions shown as higher magnification inset images. (B) Segmentation of hyphal shapes and detection of growing poles using our image analysis platform (green box for the growing tip signal, red box for the non-growing back, purple for cell sides, and blue boxes for cytoplasm). (C) Mean±s.d. growth speed of germlings ($n$=15 cells) and mature hyphae ($n$=18). ***$P$<0.001 (two-tailed Mann–Whitney test). (D) Tip growth speeds plotted as a function of GFP–RabE$^{Rab11}$ concentrations at the cell pole for both germlings and mature hyphae. Small dots in the background are single time points from individual time-lapse images. Large dots are binned averages and error bars represent the s.d. (see Materials and Methods for details on binning). A.U, arbitrary units. Scale bars: 5 µm.

## MATERIALS AND METHODS

### Yeast strains and medium

Fission yeast *Schizosaccharomyces pombe* cells were grown at room temperature in yeast extract plus five supplements (YE5S) medium (MP Biomedicals) unless otherwise indicated. Strains used in this study are listed in Table S1. For time-lapse experiments, cells were grown overnight in liquid culture at 25°C, harvested, labeled for 5 min with 5 mg/ml of lectin from *Griffonia simplicifolia* (also known as *Bandeiraea simplicifolia*) conjugated with Alexa Fluor 647 (lectin–A647; Gs-IB4–Alexa Fluor 647; ThermoFisher) and mounted on an agar pad supplemented with 5 mg/ml of lectin–A647 before being imaged directly (Davì et al., 2018).

### *Aspergillus* strain and medium

A mycelium of *Aspergillus nidulans* was grown for 5 days on malt extract (MCA, Aspergillus complete medium; MP Biomedicals) plates. Spores were collected in water supplemented with 1% Tween 20 and kept at 4°C for up to a month. For time-lapse imaging, a 1/10 dilution of spores was plated on cellophane on top of an MCA agar plate then grown overnight at 25°C. The next morning, a square of cellophane (~15×15 mm$^2$) was cut and placed on an MCA agar pad supplemented with 0.2 mg/ml of fluorescent WGA lectin (wheat germ agglutinin–Alexa Fluor 647; ThermoFisher).

### Microscopy

Live-cell imaging was performed on an inverted spinning-disk confocal microscope equipped with motorized stages and perfect focus system (Nikon Ti-Eclipse), a Yokogawa CSU-X1FW spinning head, an EM-CCD camera (Hamamatsu), a 100× oil-immersion objective (Nikon CFI Plan Apo DM 100×/1.4 NA) and a 2.5× magnifying lens, and controlled by MetaMorph (Microscopy Automation & Image Analysis Software). For yeast experiments, time-lapses were ~5–6 h long with an interval of 5 or 10 min (depending on the strain). Exposure in the blue or far-red channels were kept similar between experiments, to homogenize putative phototoxic effects and bleaching. However, in some of the dimmer signals, we increased both the exposure and time intervals, so that the total amount of light received by cells was roughly constant. Imaging was performed at room temperature (22–26°C) unless indicated otherwise, with controlled humidity (>30%). For experiments on *A. nidulans*, the objective was heated to 28°C using an objective heater (Bioptechs).

### Image analysis

To analyze growth rates of single tips and local concentrations of polar factors, we improved a previously reported dedicated MATLAB (Mathworks) image analysis platform (Davì et al., 2018; Haupt et al., 2018) (Fig. S1). We first segmented cells using the signal from the lectin-labeled cell wall. To this aim, we first smoothed the image with median and Gaussian filters and detected cell edges using the Canny edge detector. The resultant binary image was then filtered to remove small edge chunks. Given that the signal of the labeled cell wall has a finite thickness, the edges delineated the inner and the outer border of this signal. All spaces in this image were then filled in white (binary 1), except for the spaces between the inner and outer border of the wall, yielding a black band (binary 0) representing the cell wall. Using the watershed algorithm, we finally extracted the whole-cell contour defined as the middle of this band.



Journal of Cell Science

Note that in the platform, a dedicated interface allows modulation of these segmentation steps, in order to segment different types of signals (including phase contrast, DIC and fluorescence). To compute cell length, we fitted the long axis of the segmented cell with a third degree polynomial. This fit was then used to define a 'cell spine', and its length was calculated and used as a measurement for cell length. An interface then allowed us to define the cell shape more precisely, remove unwanted neighbor cells or objects and orient the NE versus the OE. The final step consisted of adjusting the spine and tracking the birth scars using a semi-automated interface, based on radius detection along the cell spine, and manual verification of scar positions. The positioning of scars allowed for the computation of elongation rates of the NE and OE.

The whole-cell contour could then be manipulated using morphological and logical operations to obtain a set of arbitrary regions (for example, tips, membrane and cytoplasm). The tip regions are, for instance, shaped as a cut off from the whole-cell mask perpendicular to the cell spine at specific distances along the spine. The background was calculated from a region surrounding the cell shape defined by dilation of the cell shape. Fluorescence signals of interest were then extracted from fluorescence images using a mask based on corresponding subregions and were background corrected. The concentration at cell tips was computed by normalizing the background-corrected tip signal with the background-corrected cytoplasm signal; allowing us to directly account for photobleaching effects.

This tracking platform is available for the community. The following download link provides a package including the image analysis method for tracking growth and polarity, precise user-friendly guidelines and examples for training: https://drive.google.com/file/d/1Fot7V0PvoFGXnYBSZMsWgEiuPIWjY6Kz/view.

Finally, a second dedicated MATLAB script was developed to compute the mean trend in cell size, tip growth speed and pole concentration over a population of single tips analyzed from the tracking platform mentioned above. Because cell cycle time can vary even within the same group of cells imaged at the same time, we rescaled the cell cycle time of each cell to the average cycle time of the genetic background.

To obtain averaged measurements (total length, OE/NE lengths, OE/NE concentration values) and their derivatives (growth speed and growth rate, computed as a local slope over a three point window) over multiple cells, we binned time in bins of 10 min in order to compute the mean behavior of the population in each bin and the standard deviation (see Fig. 1C,D for example).

To plot tip growth speed as a function of pole concentration, we used the data from individual (non-averaged) cells. We binned concentrations in a set of thirty regularly spaced bins of concentrations between zero and the maximum observed concentration and discarded bins that had fewer than five experimental time points, to limit outlier behavior. In each bin, we then computed the mean and the standard deviation of tip growth speed.

Statistical and correlation analyses were carried out using Prism 6 software (GraphPad Software, La Jolla, CA). To compute significance throughout this work, we used one-way analysis of variance (ANOVA) followed by Dunnett multiple comparisons test, or two-tailed, unpaired *t*-test. Statistically significant differences between groups is reported in the figure legends. For all experiments reported in this study, at least two independent experiments were performed.

#### Acknowledgements
We thank the Martin, Gould, Wu, Balasubramanian and Peñalva laboratories for sharing strains. We gratefully thank all members of the Minc laboratory for discussion and technical help.

#### Competing interests
The authors declare no competing or financial interests.

#### Author contributions
Conceptualization: S.T., D.E., N.M.; Methodology: S.T., D.E., S.D.; Software: D.E., S.D.; Validation: D.E.; Formal analysis: S.T., D.E., S.D., N.M.; Investigation: S.T., D.E., N.M.; Data curation: S.T., S.D.; Writing - original draft: S.T., D.E., N.M.; Writing - review & editing: S.T., D.E., S.D., N.M.; Supervision: N.M.; Project administration: N.M.; Funding acquisition: N.M.

#### Funding
This work was supported by the Centre National de la Recherche Scientifique (CNRS), the Agence Nationale de la Recherche ('Cell size'; no. ANR-14-CE11-0009-02) and the European Research Council (ERC CoG 'Forcaster'; no. 647073).

#### Supplementary information
Supplementary information available online at
https://jcs.biologists.org/lookup/doi/10.1242/jcs.252064.supplemental

#### Peer review history
The peer review history is available online at
https://jcs.biologists.org/lookup/doi/10.1242/jcs.252064.reviewer-comments.pdf

#### References
**Abenza, J. F., Couturier, E., Dodgson, J., Dickmann, J., Chessel, A., Dumais, J. and Carazo Salas, R. E.** (2015). Wall mechanics and exocytosis define the shape of growth domains in fission yeast. *Nat. Commun.* **6**, 8400. doi:10.1038/ncomms9400

**Atilgan, E., Magidson, V., Khodjakov, A. and Chang, F.** (2015). Morphogenesis of the fission yeast cell through cell wall expansion. *Curr. Biol.* **25**, 2150-2157. doi:10.1016/j.cub.2015.06.059

**Ayscough, K. R., Stryker, J., Pokala, N., Sanders, M., Crews, P. and Drubin, D. G.** (1997). High rates of actin filament turnover in budding yeast and roles for actin in establishment and maintenance of cell polarity revealed using the actin inhibitor latrunculin-A. *J. Cell Biol.* **137**, 399-416. doi:10.1083/jcb.137.2.399

**Bastmeyer, M., Deising, H. B. and Bechinger, C.** (2002). Force exertion in fungal infection. *Annu. Rev. Biophys. Biomol. Struct.* **31**, 321-341. doi:10.1146/annurev.biophys.31.091701.170951

**Baumgärtner, S. and Tolić-Nørrelykke, I. M.** (2009). Growth pattern of single fission yeast cells is bilinear and depends on temperature and DNA synthesis. *Biophys. J.* **96**, 4336-4347. doi:10.1016/j.bpj.2009.02.051

**Bendezú, F. O., Vincenzetti, V., Vavylonis, D., Wyss, R., Vogel, H. and Martin, S. G.** (2015). Spontaneous Cdc42 polarization independent of GDI-mediated extraction and actin-based trafficking. *PLoS Biol.* **13**, e1002097. doi:10.1371/journal.pbio.1002097

**Bonazzi, D., Julien, J.-D., Romao, M., Seddiki, R., Piel, M., Boudaoud, A. and Minc, N.** (2014). Symmetry breaking in spore germination relies on an interplay between polar cap stability and spore wall mechanics. *Dev. Cell* **28**, 534-546. doi:10.1016/j.devcel.2014.01.023

**Bonazzi, D., Haupt, A., Tanimoto, H., Delacour, D., Salort, D. and Minc, N.** (2015). Actin-based transport adapts polarity domain size to local cellular curvature. *Curr. Biol.* **25**, 2677-2683. doi:10.1016/j.cub.2015.08.046

**Cadart, C., Monnier, S., Grilli, J., Sáez, P. J., Srivastava, N., Attia, R., Terriac, E., Baum, B., Cosentino-Lagomarsino, M. and Piel, M.** (2018). Size control in mammalian cells involves modulation of both growth rate and cell cycle duration. *Nat. Commun.* **9**, 3275. doi:10.1038/s41467-018-05393-0

**Chang, F. and Martin, S. G.** (2009). Shaping fission yeast with microtubules. *Cold Spring Harb. Perspect. Biol.* **1**, a001347. doi:10.1101/cshperspect.a001347

**Das, M., Drake, T., Wiley, D. J., Buchwald, P., Vavylonis, D. and Verde, F.** (2012). Oscillatory dynamics of Cdc42 GTPase in the control of polarized growth. *Science* **337**, 239-243. doi:10.1126/science.1218377

**Davì, V. and Minc, N.** (2015). Mechanics and morphogenesis of fission yeast cells. *Curr. Opin. Microbiol.* **28**, 36-45. doi:10.1016/j.mib.2015.07.010

**Davì, V., Tanimoto, H., Ershov, D., Haupt, A., De Belly, H., Le Borgne, R., Couturier, E., Boudaoud, A. and Minc, N.** (2018). Mechanosensation dynamically coordinates polar growth and cell wall assembly to promote cell survival. *Dev. Cell* **45**, 170-182.e7. doi:10.1016/j.devcel.2018.03.022

**Davì, V., Chevalier, L., Guo, H., Tanimoto, H., Barrett, K., Couturier, E., Boudaoud, A. and Minc, N.** (2019). Systematic mapping of cell wall mechanics in the regulation of cell morphogenesis. *Proc. Natl. Acad. Sci. USA* **116**, 13833-13838. doi:10.1073/pnas.1820455116

**Di Gregorio, A., Bowling, S. and Rodriguez, T. A.** (2016). Cell competition and its role in the regulation of cell fitness from development to cancer. *Dev. Cell* **38**, 621-634. doi:10.1016/j.devcel.2016.08.012

**Haupt, A., Ershov, D. and Minc, N.** (2018). A positive feedback between growth and polarity provides directional persistency and flexibility to the process of tip growth. *Curr. Biol.* **28**, 3342-3351.e3. doi:10.1016/j.cub.2018.09.022

**Horio, T. and Oakley, B. R.** (2005). The role of microtubules in rapid hyphal tip growth of Aspergillus nidulans. *Mol. Biol. Cell* **16**, 918-926. doi:10.1091/mbc.e04-09-0798

**Horiseberger, M. and Rosset, J.** (1977). Localization of α-Galactomannan on the surface of Schizosaccharomyces pombe cells by scanning electron microscopy. *Arch. Microbiol.* **112**, 123-126. doi:10.1007/BF00429323

**Horváth, A., Rácz-Mónus, A., Buchwald, P. and Sveiczer, Á.** (2013). Cell length growth in fission yeast: an analysis of its bilinear character and the nature of its rate change transition. *FEMS Yeast Res.* **13**, 635-649. doi:10.1111/1567-1364.12064

**Howell, A. S., Savage, N. S., Johnson, S. A., Bose, I., Wagner, A. W., Zyla, T. R., Nijhout, H. F., Reed, M. C., Goryachev, A. B. and Lew, D. J.** (2009). Singularity

in polarization: rewiring yeast cells to make two buds. *Cell* **139**, 731-743. doi:10.1016/j.cell.2009.10.024

**Kelkar, M. and Martin, S. G.** (2015). PKA antagonizes CLASP-dependent microtubule stabilization to re-localize Pom1 and buffer cell size upon glucose limitation. *Nat. Commun.* **6**, 8445. doi:10.1038/ncomms9445

**Kinnaer, C., Dudin, O. and Martin, S. G.** (2019). Yeast-to-hypha transition of Schizosaccharomyces japonicus in response to environmental stimuli. *Mol. Biol. Cell* **30**, 975-991. doi:10.1091/mbc.E18-12-0774

**Klumpp, S., Scott, M., Pedersen, S. and Hwa, T.** (2013). Molecular crowding limits translation and cell growth. *Proc. Natl Acad. Sci. USA* **110**, 16754-16759. doi:10.1073/pnas.1310377110

**Knapp, B. D., Odermatt, P., Rojas, E. R., Cheng, W., He, X., Huang, K. C. and Chang, F.** (2019). Decoupling of rates of protein synthesis from cell expansion leads to supergrowth. *Cell Syst.* **9**, 434-445.e6. doi:10.1016/j.cels.2019.10.001

**Köhli, M., Galati, V., Boudier, K., Roberson, R. W. and Philippsen, P.** (2008). Growth-speed-correlated localization of exocyst and polarisome components in growth zones of *Ashbya gossypii* hyphal tips. *J. Cell Sci.* **121**, 3878-3889. doi:10.1242/jcs.033852

**Lew, R. R.** (2011). How does a hypha grow? The biophysics of pressurized growth in fungi. *Nat. Rev. Microbiol.* **9**, 509-518. doi:10.1038/nrmicro2591

**Loewith, R. and Hall, M. N.** (2011). Target of rapamycin (TOR) in nutrient signaling and growth control. *Genetics* **189**, 1177-1201. doi:10.1534/genetics.111.133363

**López-Franco, R., Bartnicki-Garcia, S. and Bracker, C. E.** (1994). Pulsed growth of fungal hyphal tips. *Proc. Natl Acad. Sci. USA* **91**, 12228-12232. doi:10.1073/pnas.91.25.12228

**Martin, S. G.** (2015). Spontaneous cell polarization: feedback control of Cdc42 GTPase breaks cellular symmetry. *BioEssays* **37**, 1193-1201. doi:10.1002/bies.201500077

**Martin, S. G. and Arkowitz, R. A.** (2014). Cell polarization in budding and fission yeasts. *FEMS Microbiol. Rev.* **38**, 228-253. doi:10.1111/1574-6976.12055

**Minc, N., Boudaoud, A. and Chang, F.** (2009). Mechanical forces of fission yeast growth. *Curr. Biol.* **19**, 1096-1101. doi:10.1016/j.cub.2009.05.031

**Mitchison, J. M. and Nurse, P.** (1985). Growth in cell length in the fission yeast Schizosaccharomyces pombe. *J. Cell Sci.* **75**, 357-376.

**Neurohr, G. E., Terry, R. L., Lengefeld, J., Bonney, M., Brittingham, G. P., Moretto, F., Miettinen, T. P., Vaites, L. P., Soares, L. M., Paulo, J. A. et al.** (2019). Excessive cell growth causes cytoplasm dilution and contributes to senescence. *Cell* **176**, 1083-1097.e18. doi:10.1016/j.cell.2019.01.018

**Nobs, J.-B. and Maerkl, S. J.** (2014). Long-term single cell analysis of S. pombe on a microfluidic microchemostat array. *PLoS ONE* **9**, e93466. doi:10.1371/journal.pone.0093466

**Pantazopoulou, A., Pinar, M., Xiang, X. and Peñalva, M. A.** (2014). Maturation of late Golgi cisternae into RabERAB11 exocytic post-Golgi carriers visualized in vivo. *Mol. Biol. Cell* **25**, 2428-2443. doi:10.1091/mbc.e14-02-0710

**Peñalva, M. A., Zhang, J., Xiang, X. and Pantazopoulou, A.** (2017). Transport of fungal RAB11 secretory vesicles involves myosin-5, dynein/dynactin/p25, and kinesin-1 and is independent of kinesin-3. *Mol. Biol. Cell* **28**, 947-961. doi:10.1091/mbc.e16-08-0566

**Perez, P. and Cansado, J.** (2010). Cell integrity signaling and response to stress in fission yeast. *Curr. Protein Pept. Sci.* **11**, 680-692. doi:10.2174/138920310794557718

**Perez, P. and Ribas, J. C.** (2004). Cell wall analysis. *Methods* **33**, 245-251. doi:10.1016/j.ymeth.2003.11.020

**Perez-Gonzalez, N. A., Rochman, N. D., Yao, K., Tao, J., Le, M.-T. T., Flanary, S., Sablich, L., Toler, B., Crentsil, E., Takaesu, F. et al.** (2019). YAP and TAZ regulate cell volume. *J. Cell Biol.* **218**, 3472-3488. doi:10.1083/jcb.201902067

**Qin, Y. and Yang, Z.** (2011). Rapid tip growth: insights from pollen tubes. *Semin. Cell Dev. Biol.* **22**, 816-824. doi:10.1016/j.semcdb.2011.06.004

**Riquelme, M. and Bartnicki-Garcia, S.** (2004). Key differences between lateral and apical branching in hyphae of Neurospora crassa. *Fungal Genet. Biol.* **41**, 842-851. doi:10.1016/j.fgb.2004.04.006

**Riquelme, M., Aguirre, J., Bartnicki-García, S., Braus, G. H., Feldbrügge, M., Fleig, U., Hansberg, W., Herrera-Estrella, A., Kämper, J., Kück, U. et al.** (2018). Fungal morphogenesis, from the polarized growth of hyphae to complex reproduction and infection structures. *Microbiol. Mol. Biol. Rev.* **82**, e00068-17. doi:10.1128/MMBR.00068-17

**Russell, P. and Nurse, P.** (1986). cdc25+ functions as an inducer in the mitotic control of fission yeast. *Cell* **45**, 145-153. doi:10.1016/0092-8674(86)90546-5

**Soifer, I., Robert, L. and Amir, A.** (2016). Single-cell analysis of growth in budding yeast and bacteria reveals a common size regulation strategy. *Curr. Biol.* **26**, 356-361. doi:10.1016/j.cub.2015.11.067

**Son, S., Tzur, A., Weng, Y., Jorgensen, P., Kim, J., Kirschner, M. W. and Manalis, S. R.** (2012). Direct observation of mammalian cell growth and size regulation. *Nat. Methods* **9**, 910-912. doi:10.1038/nmeth.2133

**Steinberg, G., Peñalva, M. A., Riquelme, M., Wosten, H. A. and Harris, S. D.** (2017). Cell biology of hyphal growth. *Microbiol. Spectr.* **5**, eFUNK-0034-2016. doi:10.1128/microbiolspec.FUNK-0034-2016

**Tatebe, H., Nakano, K., Maximo, R. and Shiozaki, K.** (2008). Pom1 DYRK regulates localization of the Rga4 GAP to ensure bipolar activation of Cdc42 in fission yeast. *Curr. Biol.* **18**, 322-330. doi:10.1016/j.cub.2008.02.005

**Uyttewaal, M., Burian, A., Alim, K., Landrein, B., Borowska-Wykręt, D., Dedieu, A., Peaucelle, A., Ludynia, M., Traas, J., Boudaoud, A. et al.** (2012). Mechanical stress acts via katanin to amplify differences in growth rate between adjacent cells in arabidopsis. *Cell* **149**, 439-451. doi:10.1016/j.cell.2012.02.048

**Weiss, R. L., Kukora, J. R. and Adams, J.** (1975). The relationship between enzyme activity, cell geometry, and fitness in Saccharomyces cerevisiae. *Proc. Natl Acad. Sci. USA* **72**, 794-798. doi:10.1073/pnas.72.3.794

**Wu, C.-F. and Lew, D. J.** (2013). Beyond symmetry-breaking: competition and negative feedback in GTPase regulation. *Trends Cell Biol.* **23**, 476-483. doi:10.1016/j.tcb.2013.05.003

**Yuan, H.-X., Xiong, Y. and Guan, K.-L.** (2013). Nutrient sensing, metabolism, and cell growth control. *Mol. Cell* **49**, 379-387. doi:10.1016/j.molcel.2013.01.019

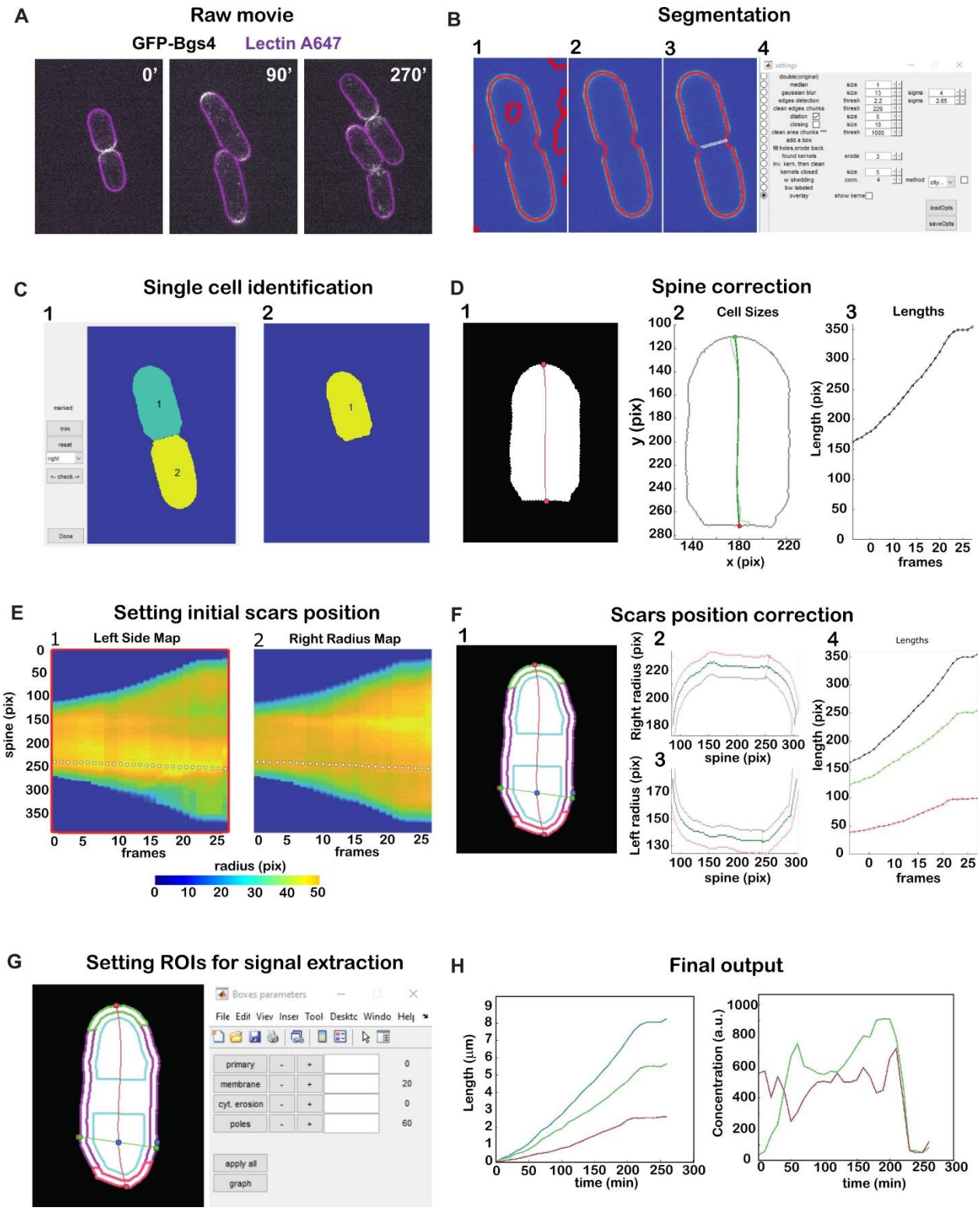
A
Raw movie
GFP-Bgs4
Lectin A647
0'
90'
270'
B
Segmentation
1
2
3
4
C
Single cell identification
1
2
D
Spine correction
1
2
Cell Sizes
y (pix)
x (pix)
3
Lengths
Length (pix)
frames
E
Setting initial scars position
1
Left Side Map
2
Right Radius Map
spine (pix)
frames
radius (pix)
F
Scars position correction
1
2
Right radius (pix)
spine (pix)
3
Left radius (pix)
4
Lengths
G
Setting ROIs for signal extraction
Boxes parameters
primary
membrane
cyt. erosion
poles
apply all
graph
H
Final output
Length (μm)
time (min)
Concentration (a.u.)
time (min)

**Figure S1. Image analysis workflow. (A)** Raw images have two signals: one from labeled cell walls (Lectin-A647), which we use to segment the cells, and the other from labeled proteins of interest (i.e. GFP-Bgs4). The image analysis package provides a first tool for organization of the input data into separate stage positions, adapted to Metamorph outputs. **(B)** Segmentation. The program aims to delineate cells present in the field of view using the signal of the stained cell wall, or other signals (Bright field, phase, DIC..). Initial segmentation is typically not good (1), and the user needs to adjust a number of parameters (3) to get a good segmentation (2). In case when it is not possible to get proper deliniation (weak contour signal), the user can draw edges manually; this happens often for the separation between young daughter cells, since there is not enough Lectin signal at the division site (4). **(C)** Identification of individual cells. The user chooses a cell of interest (i.e. "1") and removes the unwanted segment ("2" and others if present). The tool provides the means to quickly remove unwanted ROIs from the whole time lapse). Importantly, in this step the direction of the new end is set; this information is used in the following analysis to distinguish the poles. **(D)** Spine correction. The total length of the current cell is calculated form the central line of the ROI ("spine"). The position of the endpoints of this line can be revised manually if required. **(E)** Setting initial scars position. In this step the user sees a 2D surface; the x-dimension is time, the y-dimension is cell length, and the colored intensity (blue = low, yellow = high) is the radius of a cell to the left of the spine (1) and to the right (2). The wider radii corresponding to the scar location should appear brighter in these surfaces, and the user manually draws a line (shown with small white circles) thus setting the scar position for the whole time lapse. **(F)** Scar position correction. The software provides a tool to correct manually the positions of the endpoints of each scar. Radii profiles (1,2) are used as the reference for positioning the scars; the curves showing the evolution of lengths in time (green curve for the old end and red curve for the new end) can also help guiding scar positioning. **(G)** Setting ROIs for signal extraction. The user can set the sizes of various ROIs: the membrane width (purple), old/new end ROI along the spine (green/red), and cytoplasm (cyan). **(H)** Typical data output for cell length (OE in green, NE in red and total cell length in blue) and polarity concentration evolution at both ends in a single cell.

Journal of Cell Science • Supplementary information

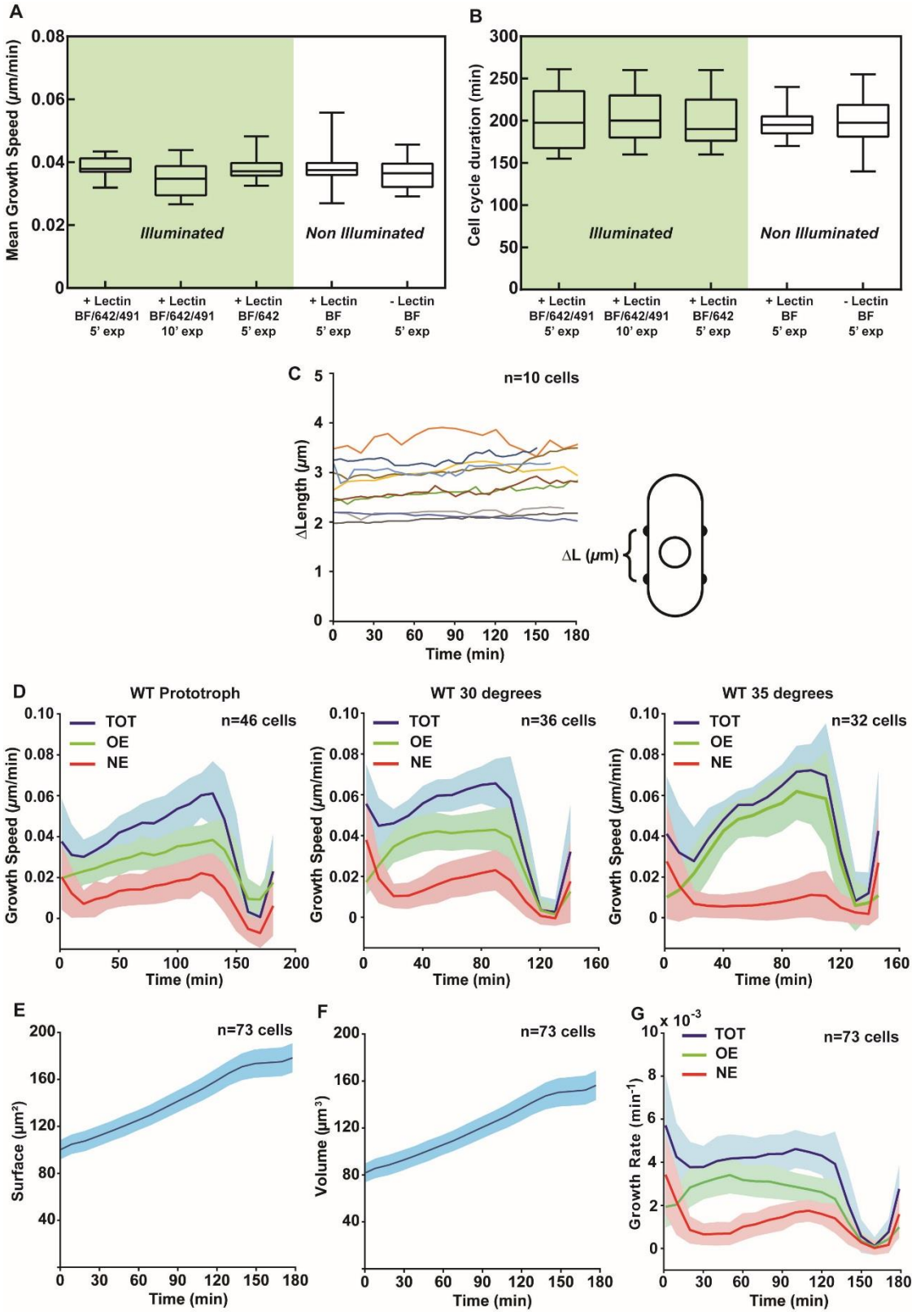


Journal of Cell Science • Supplementary information

**Figure S2. Controls for the imaging and image analysis methodology, and impact of temperature and auxotrophies on growth speeds. (A)** Mean growth speeds of cells imaged under the indicated conditions (n > 20 cells for each conditions). **(B)** Mean cell cycle time (computed from the end of septation to the end of the next septation), for cells imaged under the indicated conditions (n > 20 cells for each conditions). Error bars represent standard deviations. **(C)** Evolution of the distance between two birth scars plotted as a function of time over the cell cycle for 10 individual cells (represented by a different color). **(D)** Growth speed for the OE, NE and total cell of a WT prototroph strain (n=46 cells, left), a WT laboratory strain grown at 30°C (n=36, middle) and a WT laboratory strain grown at 35°C (n=32, middle). The dark line represent the average and colored shades delimit +/- the standard deviation. **(E-F)** Evolution of the surface and volume along the cell cycle, computed as the sum of the perimeter or area, respectively, of cross sections along the cell spline axis (n=73 cells). (G) Growth rate computed as the growth speed divided by cell length for the OE, NE and total length of WT cells (n=73 cells).

Journal of Cell Science • Supplementary information

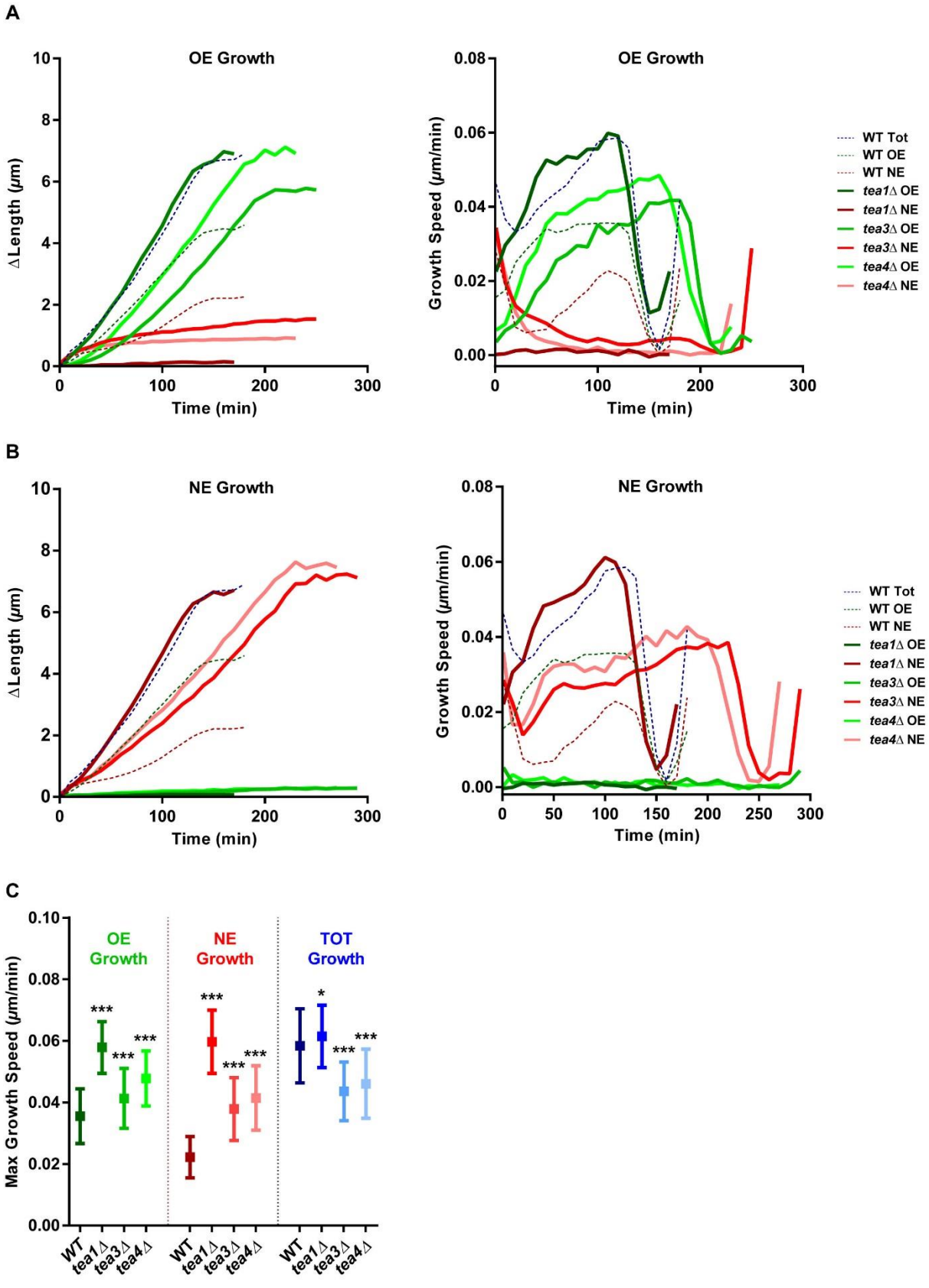


Journal of Cell Science • Supplementary information

**Figure S3. Tip growth speeds of monopolar tea mutants. (A)** Comparison of Total, OE and NE lengths expansions and Growth Speed (GS) of WT (dotted lines, n=73 cells) and *tea1Δ* (n=16), *tea3Δ* (n=12) and *tea4Δ* (n=25) old end growing cells during the cell cycle. **(B)** Comparison of Total, OE and NE lengths expansions and Growth Speed (GS) of WT (dotted lines, n=73 cells) and *tea1Δ* (n=35), *tea3Δ* (n=10) and *tea4Δ* (n=14) new end growing cells during the cell cycle. (C) Mean maximum growth speed, computed as an average on 20min around the maximum of the speed profile, for the indicated mutant and tips. Results between genotypes for OE, NE and total growth were compared by using a two-tailed Mann–Whitney test. *, $P < 0.1$; **, $P < 0.01$; ***, $P < 0.001$. Error bars are standard deviations.

Journal of Cell Science • Supplementary information

**Table S1. Strains used in this study**

| IDENTIFIER | Mat Type | Genotype | Auxtotrophy | Source |
|---|---|---|---|---|
| NM291 | h- | WT | ALU- | Lab stocks |
| NM439 | h- | GFP-atb2:KanMX | LU- | Lab stocks |
| NM123 | h- | CRIB-GFP:Ura | ALU | Lab stocks |
| NM256 | h+ | bgs4::ura4 GFP-bgs4-Leu | LUH- | Lab stocks |
| NM244 | h+ | rlc1-GFP:KanMX | ALU- | Lab stocks |
| NM04 | h+ | cdc25-22 | ALU- | Lab stocks |
| NM299 | h+ | tea1::ura4 | AL- | Lab stocks |
| DE040 | h- | tea3::KanMX | ALU- | Lab stocks |
| DB162 | h+ | tea4::KanMX | ALU- | Lab stocks |
| NM341 | h+ | tea1-3GFP-KanMX | LU- | Lab stocks |
| DE039 | h+ | tea4-GFP:KanMX | ALU- | Lab stocks |
| DE003 | h- | pom1-GFP-kanMX | AL- | Martin lab (University of Lausanne, Switzerland) |
| NM311 | h- | for3-3GFP-ura4 | ALU- | Lab stocks |
| NM335 | h- | bud6-3GFP-KanMX | ALU- | Lab stocks |
| DB332 | h- | Pact1-LAGFP:leu1+ | UL | Balasubramaian lab (U. Warwick, UK) |
| AH282 | h- | leu1::KanMX6-P3nmt1-pkc1(HR1-C2)-mECitrine | ALU- | Wu lab (Ohio State University, USA) |
| ST43 | h- | rgf1-GFP:kanR | ALU- | Gould lab (Vanderbilt Univeristy, USA) |
| DE005 | h- | sec8-GFP-ura4+ | L- | Martin lab (University of Lausanne, Switzerland) |
| NM253 | h- | bgs1::ura4 GFP-bgs1-Leu | LUH- | Lab stocks |
| ST15 | h- | myo52-3GFP::KanMX | ALU- | Lab stocks |
| NM348 | h- | tea1::NatMX bgs4::ura4 GFP-bgs4-Leu | AL- | Lab stocks |
| AH151 | h- | tea1::NatMX CRIB-3GFP:ura | | Lab stocks |
| ST31 | h+ | tea1::ura4 Pact1-LAGFP:leu1+ | A- | Lab stocks |
| ST45 | h+ | tea1::ura4 rgf1-GFP:kanR | AL- | This study |
| | | | | |
| MAD5933 | *A. nidulans* | RabEp::GFP-RabE::pyrGAf, pyroA4, pyrG89, nkuAΔ::bar? | | Peñalva lab (University of Madrid, Spain) |

Journal of Cell Science • Supplementary information